Journal of Zhejiang University-SCIENCE A (Applied Physics & Engineering) 2023 24(6):473-496
www.jzus.zju.edu.cn; www.springer.com/journal/11582
E-mail: jzus_a@zju.edu.cn

Research Article

https://doi.org/10.1631/jzus.A2200565

Investigation of flow characteristics in a rotor-stator cavity under crossflow using wall-modelled large-eddy simulation

Lei XIE[1,2,3], Qiang DU[1,2,3]✉, Guang LIU[1,2,3], Zengyan LIAN[1,2,3], Yaguang XIE[1,2,3], Yifu LUO[1,2,3]

[1]*Key Lab of Light-duty Gas-turbine, Institute of Engineering Thermophysics, Chinese Academy of Sciences, Beijing 100190, China*
[2]*University of Chinese Academy of Sciences, Beijing 100049, China*
[3]*Innovation Academy for Light-duty Gas Turbine, Chinese Academy of Sciences, Beijing 100190, China*

Abstract: Rotor-stator cavities are frequently encountered in engineering applications such as gas turbine engines. They are usually subject to an external hot mainstream crossflow which in general is highly swirled under the effect of the nozzle guide vanes. To avoid hot mainstream gas ingress, the cavity is usually purged by a stream of sealing flow. The interactions between the external crossflow, cavity flow, and sealing flow are complicated and involve all scales of turbulent unsteadiness and flow instability which are beyond the resolution of the Reynolds-average approach. To cope with such a complex issue, a wall-modeled large-eddy simulation (WMLES) approach is adopted in this study. In the simulation, a 20° sector model is used and subjected to a uniform pre-swirled external crossflow and a stream of radial sealing flow. It is triggered by a convergent Reynolds-averaged Navier-Stokes (RANS) result in which the shear stress transport (SST) turbulent model is used. In the WMLES simulation, the Smagoringsky sub-grid scale (SGS) model is applied. A scalar transportation equation is solved to simulate the blending and transportation process in the cavity. The overall flow field characteristics and deviation between RANS and WMLES results are discussed first. Both RANS and WMLES results show a Batchelor flow mode, while distinct deviation is also observed. Deviations in the small-radius region are caused by the insufficiency of the RANS approach in capturing the small-scale vortex structures in the boundary layer while deviations in the large-radius region are caused by the insufficiency of the RANS approach in predicting the external crossflow ingestion. The boundary layer vortex and external ingestion are then discussed in detail, highlighting the related flow instabilities. Finally, the large-flow structures induced by external flow ingress are analyzed using unsteady pressure oscillation signals.

Key words: Wall-modeled large-eddy simulation (WMLES); Rotor-stator cavity; Flow instability; Reynolds-averaged Navier-Stokes (RANS)

1 Introduction

In modern gas turbines, gaps are required between stationary parts and rotating parts to accommodate the relative motion (Royce, 2015). This inevitable gap may lead to the hot mainstream gas, driven by pressure difference, ingesting into the wheel space cavity formed by the turbine disc and its adjacent casing. If not prevented, the ingested hot gas will cause serious problems such as creep, oxidation, and thermal fatigue, decreasing the life span of the turbine components. A stream of sealing flow is therefore bled from the compressor and fed into the turbine disc cavity. This stream of air cools the cavity, and at the same time pressurizes the wheel space cavity to decrease the possibility of hot gas ingestion.

Due to the influence of the injected external air and the introduced sealing air, the flow characteristics inside the rotor-stator cavity are quite complicated involving 3D and different kinds of unsteadiness, making the flow analysis extremely difficult.

Two types of external gas ingestion mechanisms have been identified by Owen (2011a, 2011b): the rotationally induced ingestion (RI) and the externally induced ingestion (EI). The RI is related to the intrinsic flow characteristics inside the wheel space cavity and occurs even if there is no external perturbation. As summarized by Owen (2011a, 2011b), the flow inside the turbine wheel space cavity shows a typical

✉ Qiang DU, duqiang@iet.cn
Qiang DU, https://orcid.org/0000-0002-8006-3778

Received Nov. 27, 2022; Revision accepted Feb. 21, 2023;
Crosschecked Mar. 19, 2023; Online first May 22, 2023

Batchelor flow mode which is governed by a viscous pumping effect at the rotor plate and a boundary layer entrainment at the stator plate. A large-scale gas recirculation is formed inside the wheel space cavity. It consists of three parts: a rotating core, an Ekman boundary layer at the rotor side, and a Boderwat boundary layer at the stator side (Childs, 2011). Due to the viscous pumping effect, fluid flows outwards into the mainstream annulus near the rotor plate, and the external gas is entrained into the cavity to supplement the egress air.

The externally induced ingestion is related to the non-axisymmetric pressure distribution in the mainstream annulus hub region induced by the nozzle guide vane wake and the potential effect of the rotor blade. Sangan et al. (2013) proposed that the mainstream flow has a highly swirled component. A non-uniform pressure field is induced due to the interaction of vanes and blades. As a result, ingress happens in the high-pressure region, and egress happens in the low-pressure region.

Hot gas ingestion has been investigated extensively using theoretical, numerical, and experimental approaches. Early experimental studies mainly focused on the determination of the minimum required sealing flow and simplified generic experiments were carried out by neglecting the external flow. Bayley and Owen (1970) investigated the effect of the superimposed radial flow on rotor-stator cavities. Predictions on drag torque and pressure were made using boundary layer approximation and compared with experimental data. Bhavnani et al. (1992) carried out an experiment on rotor-stator cavities with a double toothed rim seal in the absence of an external flow and confirmed that the differential pressure across the rim seal can be used to detect external ingestion. Phadke and Owen (1988a, 1988b, 1988c) carried out research on the aerodynamics in rotor-stator cavities. Pressure, concentration, and flow visualization measurements were made in a shrouded rotor-stator cavity, and different shroud geometries were considered.

Later, improvements were made by taking the influence of the mainstream vanes and blades into consideration. Sangan (2011) constructed an engineering gas turbine wheel space test rig and investigated the sealing effectiveness and hot gas ingestion thermal effects in the turbine cavity. Scobie (2014) also carried out research using concentration measurements and correlated the sealing effectiveness using a theoretical orifice model. Hualca-Tigsilema (2020) investigated the re-ingestion of upstream egress in turbine cavities and evaluated the re-ingestion for different sealing flow rates. In these stages, correlations of the minimum required sealing flow were obtained and used for a rough estimate in the designing process. However, these correlations cannot provide any information on the impact of the unsteady interaction inside the wheel space cavity and gave no further insight into the flow mechanism.

In theoretical investigation, Owen et al. (2012a, 2012b) developed a simple orifice model based on inviscid assumption and free vortex theorem. The model involved two separate discharge coefficients for ingress and egress to account for the viscous modification. Savov and Atkins (2017) proposed a turbulent transportation model based on a mixing length analogy. It viewed ingress and egress as turbulent diffusion and involved the determination of a turbulent diffusive coefficient. These models show good agreement with the experimental results, while experimental measurements are required in advance to determine the unknown coefficients.

Aside from experimental and theoretical research, numerical simulation approaches are used extensively with the development of computation technology. Early studies were mainly based on the Reynolds-averaged Navier-Stokes (RANS) and unsteady RANS (URANS) approaches due to their low computation costs. Jakoby et al. (2004) was the first to identify the large-scale flow structures inside the cavity. Similar results were reported by Rabs et al. (2009), Savov et al. (2017), and Horwood et al. (2019). Although considerable improvements in detailed insights of flow field have been gained, the complex unsteady flow mechanism is still not fully understood due to the resolution limit of the RANS/URANS approach. In RANS/URANS simulation, turbulent eddies in all length scales are modeled. As a result, the RANS/URANS simulation is very reliant on the choice of turbulent model, and many of the unsteady flow details are filtered. The sealing effectiveness solved by the transport equation in the RANS/URANS simulation is not accurately predicted.

Now, high-fidelity simulation methods are becoming feasible in applications such as large-eddy simulation (LES), direct numerical simulation (DNS), and the

spectral/hp element method. In the LES simulation, most turbulent eddies are resolved except for those under the Kolmogorov scale which are modeled by sub-grid scale (SGS) models (Georgiadis et al., 2010). O'Mahoney et al. (2011) carried out LES using a 13.3-degree sector model and compared the result with URANS simulation. It turned out that more hot gas ingestion is observed in LES results, but still less than in experimental results. Pogorelov et al. (2018) carried out a full circle LES simulation for an axial and radial sealing structure and analyzed the instantaneous and time-averaged flow field in detail. Large flow structures and unsteadiness were reported in the paper. The DNS method has also been reported in the open literature in turbomachinery research. Naung et al. (2021) reported a DNS simulation in predicting the flutter effect of a low-pressure turbine cascade, and Nakhchi et al. (2022) investigated the blade vibration using DNS. They all reported an excellent agreement with experimental data. Smaller-scale flow structures are resolved, providing a deeper insight into the underlying flow mechanism.

Although high-fidelity simulation methods provide a more detailed flow field solution, the computation process is still costly at an order of O (Re_τ^2) especially at high Reynolds numbers (Larsson et al., 2016).

An approximate approach referred to as wall-modeled LES (WMLES) is introduced. In the WMLES approach, the wall shear stress is modeled using correlation in the inner boundary layer, and the turbulent eddy scale larger than the inner boundary layer scale is resolved. Comparing wall-resolved LES (WRLES) and WMLES, Larsson et al. (2016) concluded that although some loss of accuracy in using wall-modeling is found, many aspects of the boundary layer flows were well preserved. Using the WMLES approach, the computation cost is very much reduced compared to conventional WRLES.

A number of previous studies have adopted WMLES in their simulation and reached a good agreement with the experimental results (Larsson et al., 2016; Palermo et al., 2020; Gao and Chewss, 2021). In turbomachinery investigations, the blade-vane interference is complicated and involves all kinds of unsteadiness, which are time-consuming to resolve. In the present study, the guiding influence of the nozzle guide vane is sorted out and investigated independently by considering a uniform pre-swirled external crossflow in the mainstream duct. WMLES is adopted to evaluate the unsteadiness and turbulent blending inside the computation domain.

This paper is organized as follows: Section 2 describes the numerical simulation method used in this study, a detailed analysis of the simulation results is presented in Section 3, and finally several conclusions are drawn and listed in Section 4.

2 Computation model and method

2.1 Geometric configuration

A typical rim sealing arrangement involves a mainstream duct with nozzle guide vanes (NGV) and turbine blades mounted and a wheel space cavity formed by a stationary disk and a rotating disk. The interaction between NGV and turbine blade creates different kinds of turbulent perturbance. These perturbances are coupled together, making the flow field very complicated. To simplify the investigation, the swirling effect of the NGV is extracted and considered independently here.

The flow configuration considered as shown in Fig. 1a is composed of a mainstream duct and a rotor-stator cavity. At the bottom of the rotor-stator cavity, a stream of sealing flow is introduced to prevent possible external crossflow ingress. On top of the rotor-stator cavity, the axial rim seal structure is mounted. The detailed geometric parameters can be referred to in Fig. 1b and Table 1. The geometric parameters of the analyzed model are in accordance with the constructing rim sealing flow characteristic test rig in the Institute of Engineering Thermophysics, Chinese Academy of Sciences.

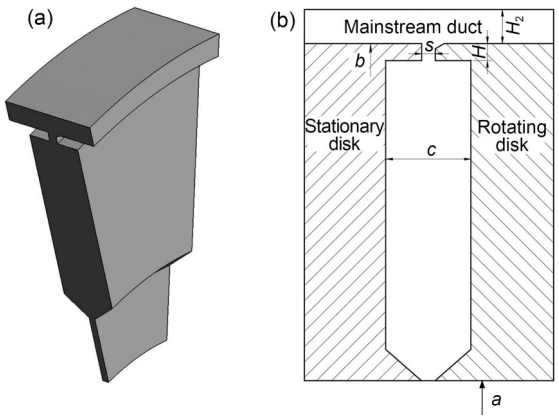

Fig. 1 Geometric configuration of the computational model: (a) computation model; (b) geometric parameters

Table 1 Detailed geometric parameters of the computational model

Geometry parameter	Value
Height of annulus, H_2 (mm)	10
Thickness of sealing lip, H (mm)	5
Outer radius of cavity, b (mm)	250
Inner radius of cavity, a (mm)	160
Axial clearance of sealing gap, s (mm)	4
Axial clearance of cavity, c (mm)	25

2.2 Computational fluid dynamics (CFD) method

Using the flow configuration, wall-resolved RANS and WMLES results are presented and compared. The WMLES simulation is initialized by a steady RANS result. All the simulations are performed by a commercial solver, ANSYS CFX v.19.

To save computational resources and speed up the convergence process, a 20° sector model is used as the computation domain. The 20° sector model has been verified to be capable of capturing the main flow characteristics in the wheel space cavity for a simple axial rim seal in previous study (Xie et al., 2021).

To monitor the blending and transportation process in the computation domain, a passive scalar transport equation is added in the simulation. In the scalar transport equation, the sealing flow concentration c_s is set to be 1 and the external crossflow concentration c_e is set to be 0. As a result, the sealing effectiveness η can be calculated by the gas concentration fraction c_∞ in the computation domain using Eq. (1). Since $c_e=0$ and $c_s=1$, η equals c_∞ in the current case.

$$\eta=\frac{c_\infty-c_e}{c_s}. \tag{1}$$

2.3 CFD setup

Structured mesh is generated using ANSYS ICEM CFD v. 19. Due to the different mesh requirements of RANS and WMLES, two sets of grids are used as shown in Figs. 2a and 2b. As shown in Fig. 2a, the RANS mesh uses refined boundary layer cells at the walls, while the WMLES mesh uses coarse quasi-isotropic cells as shown in Fig. 2b.

Meanwhile, the WMLES mesh involves prescribing the recommended cell dimensions at the wall. The y^+ value in WMLES mesh is recommended at the order of O (100), with about 20 cells to discretize the wall boundary layer, which is larger than for a WRLES mesh which requires y^+ at the order of O (1). The parallel wall grid size (i.e., r^+ and $(r\theta)^+$ in a cylinder frame of reference) is suggested to be 2–3 times y^+. This specific wall grid treatment in WMLES brings two benefits: (1) the grid number is significantly reduced compared to a conventional WRLES mesh, and (2) owing to the larger grid size, the time step in WMLES can be increased by two orders compared to WRLES since the time step is proportional to the finest grid size. As a result, the computation resource WMLES requires is much less than for WRLES. The detailed mesh information can be referred to in Table 2.

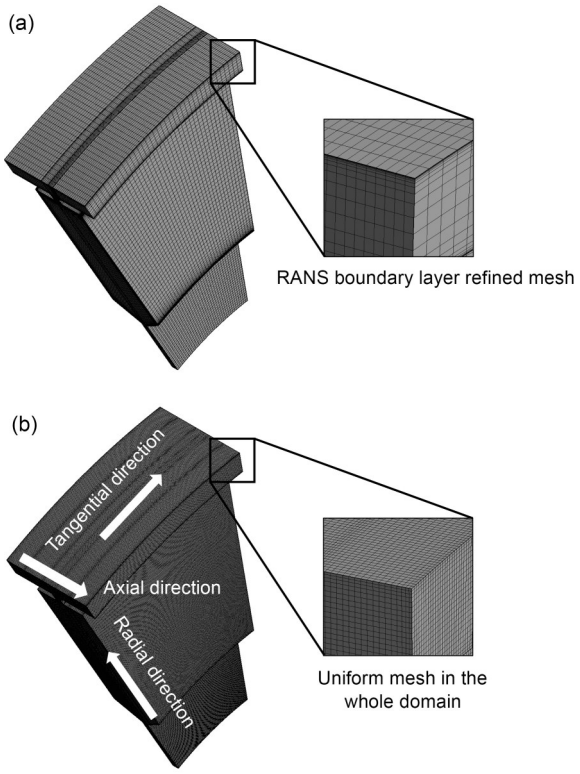

Fig. 2 RANS and WMLES grid configurations in the computation domain: (a) RANS mesh and near wall treatment; (b) WMLES mesh and near wall treatment

Table 2 Detailed parameters of RANS and WMLES meshes

Numerical method	Mesh spacing	Mesh number	First layer thickness (m)
RANS	$y^+=0.2$	641698	1×10^{-6}
WMLES	$y^+=50$, $r^+=100$, $(r\theta)^+=100$	2781945	2.3×10^{-4}

Fig. 3 shows the boundary condition settings in both RANS and WMLES simulations. In the RANS simulation, the shear stress transport (SST) turbulent model is used, and in the WMLES simulation, the Smagoringsky SGS model is used. The whole computation domain is set as a rotating domain, and a counter-rotating wall velocity is applied to the stationary walls. All the walls are set as no-slip, adiabatic, and smooth walls. The rotational periodicity boundary condition is applied to the two symmetry planes (i.e., the meridian planes). At the external flow duct inlet, the mass flow rate and inlet flow direction are specified and the static pressure is fixed at the outlet. At the seal inlet, four different sealing flow rates are considered and the mass flow rate and total temperature are specified. Detailed boundary conditions can be referred to in Table 3. The nondimensional operating parameters are listed in Table 4.

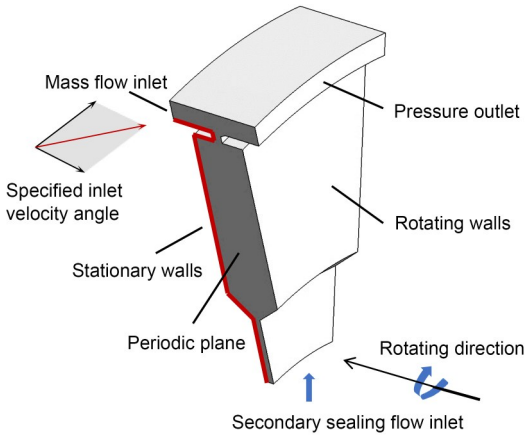

Fig. 3 Boundary conditions of the computation domain

Table 3 Detailed CFD boundary conditions

Parameter	Value
Rotating speed (r/min)	4000
Full circle mainstream flow rate (kg/s)	1.64
Air inlet angle (°)	67
Outlet static pressure (Pa)	101325
Sealing flow total temperature (K)	298.15
Full circle sealing flow rate (kg/s)	0.011–0.022–0.033–0.044

Table 4 Nondimensional operating parameters

Parameter	Value
External flow Reynolds number, Re_c	9×10^5
External flow Mach number, Ma_c	0.65
Rotational Reynolds number, Re_θ	1.62×10^6
Nondimensional sealing flow rate, c_w	2500–5000–7500–10000

In the WMLES simulation, the time step is set as 4.167×10^{-6} s based on the rotating speed of the computation domain and the finest grid size to ensure the average Courant-Friedrich-Lewy (CFL) number at the order of 1.

2.4 Numerical validation

The RANS approach has been validated by the authors in previous study (Xie et al., 2021). The WMLES approach is validated using Séverac et al. (2007)'s experimental results for an enclosed rotor-stator cavity.

The meshing strategy and CFD settings for the enclosed cavity case are the same as that introduced in Section 2.3. Séverac et al. (2007)'s geometry is depicted in Fig. 4, and the detailed geometric parameters are listed in Table 5. The computed results are time-averaged over one full rotor cycle after convergence.

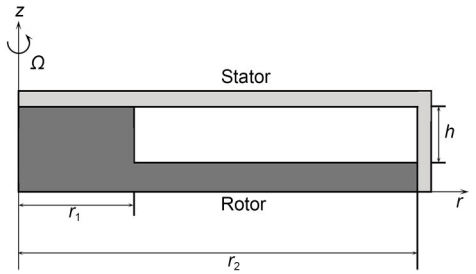

Fig. 4 Geometric configuration of the enclosed rotor-stator cavity (Séverac et al., 2007). *Ω* is the rotating speed

Table 5 Geometric parameters of the enclosed rotor-stator cavity

Parameter	Value
r_1 (mm)	40
r_2 (mm)	140
h (mm)	20

The axial swirl distributions inside the cavity at different radii are shown in Fig. 5. Both RANS and WMLES results show good agreement with the experimental results, with the WMLES result agreeing better.

2.5 Convergence verification

To monitor the unsteady flow characteristics inside the wheel space cavity, a set of monitors is inserted into the computation domain. As shown in Fig. 6, 31 monitors are radially distributed and are duplicated circumferentially by a 5° interval, indicated by column a and column b in the figure. Monitors 1–14 are

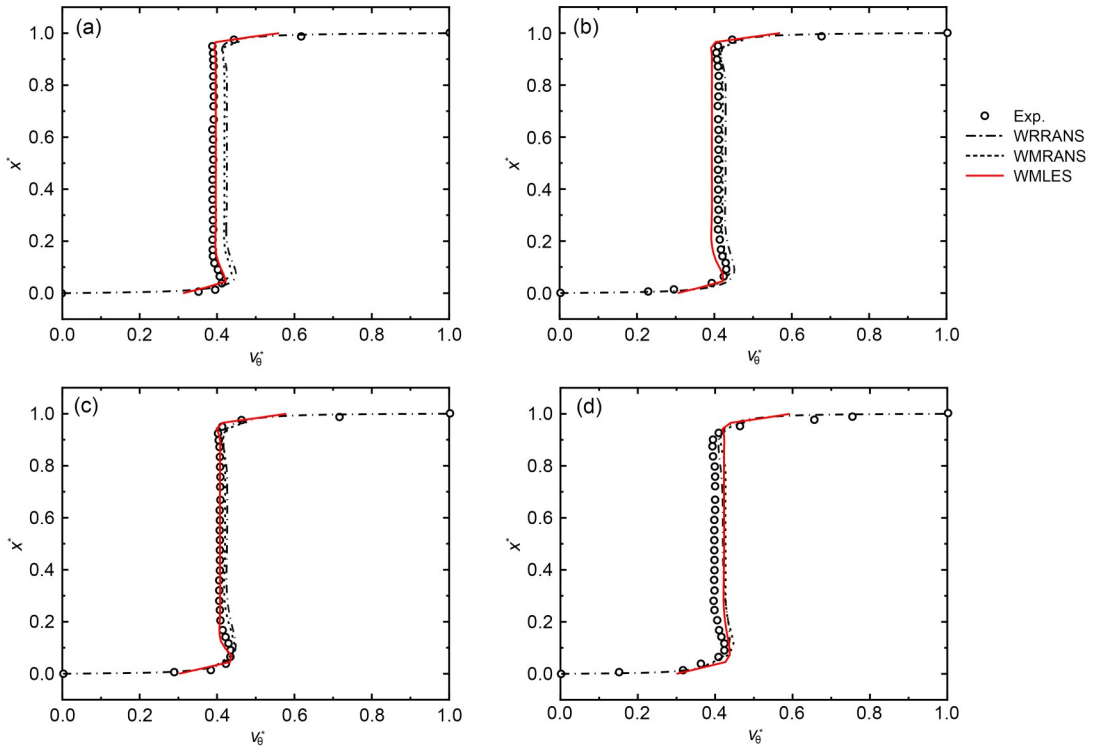

Fig. 5 Time-averaged swirl ratio in the enclosed rotor-stator cavity: (a) r^*=0.3; (b) r^*=0.5; (c) r^*=0.7; (d) r^*=0.9. x^* is the nondimensional axial position, r^* is the nondimensional radius, and v_θ^* is the nondimensional circumferential velocity

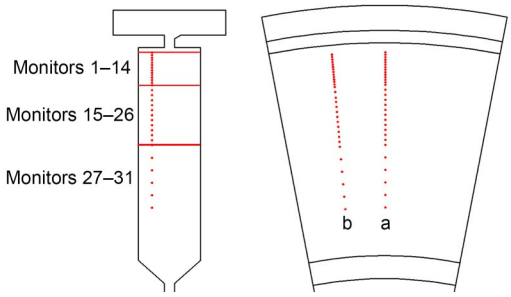

Fig. 6 Monitors in the rotor stator cavity at the x^*=0.25 plane

spaced at a 1-mm radial distance, monitors 15–26 are spaced at a 2-mm radial distance, and monitors 27–31 are spaced at a 5-mm radial distance. These monitors are set in the x^*=0.25 plane.

Final convergence is reached if (a) the root mean square error (RMSE) is less than 1×10^{-5}, (b) the pressure at the monitors fluctuates regularly, and (c) the pressure oscillation should conform with the classical Kolmogorov −5/3 scale. The convergency oscillation waves of RMSE and pressure are shown in Fig. 7, and the pressure power spectral density (PSD) is compared with the Kolmogorov −5/3 scale as shown in Fig. 8. As shown in the figures, the simulations have reached final convergence. Time averaging is performed in

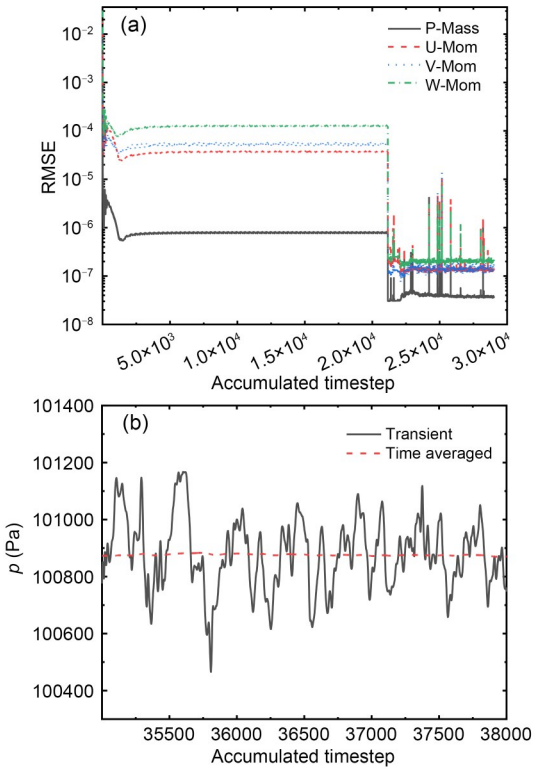

Fig. 7 RMSE (a) and pressure p (b) oscillation waves in WMLES simulation. P-Mass is the mass conservation equation; U/V/W-Mom are the three momentum equations

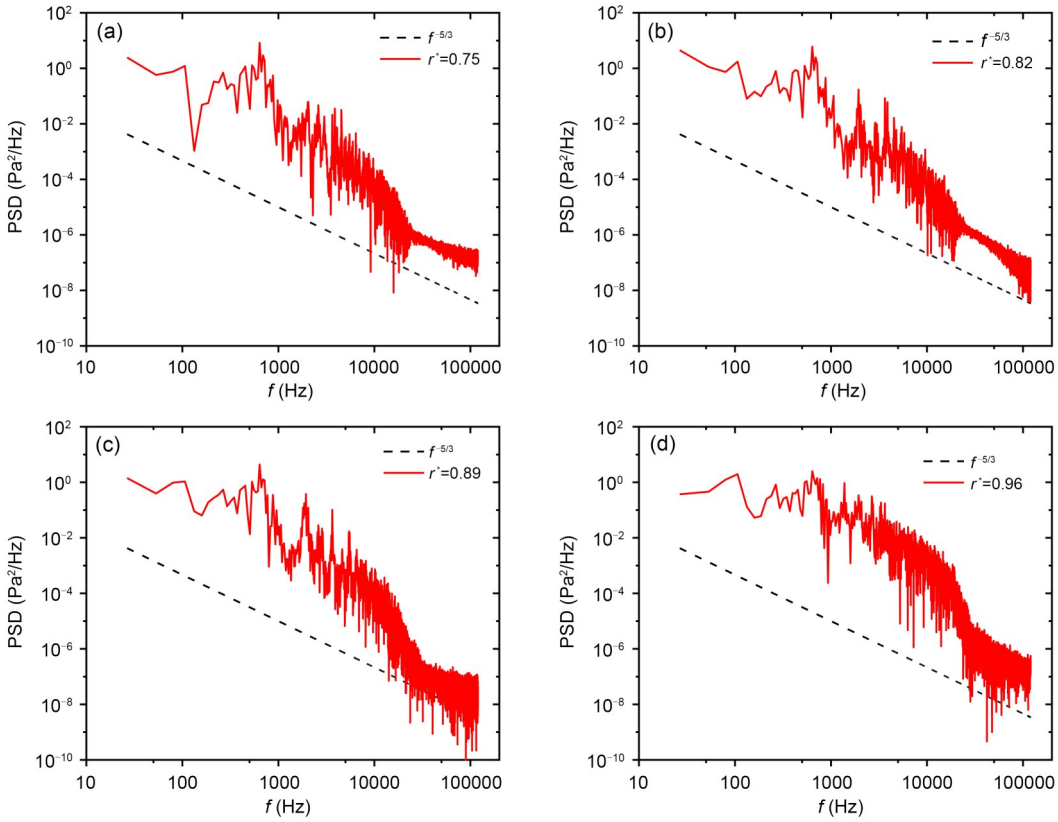

Fig. 8 Pressure PSD results compared with the Kolmogrov −5/3 scale: (a) r^*=0.75; (b) r^*=0.82; (c) r^*=0.89; (d) r^*=0.96. f is the frequency

WMLES simulation for a whole rotor cycle after final convergence is reached.

In the following sections, detailed analysis of the numerical results is presented. First, the time-averaged WMLES result is compared with the RANS result in Section 3.1. The overall flow characteristics and deviations between these two approaches are outlined. Effort is put into the investigation of the underlying mechanism causing these deviations. In Section 3.2, the centrifugal instability and crossflow instability causing the boundary layer vortex are discussed. The external crossflow ingestion and related Kelvin-Helmholtz (K-H) instability are investigated in Section 3.3. Finally in Section 3.4, the large flow structures induced by the ingress and egress are analyzed.

3 Results and discussion

3.1 Cavity overall flow characteristics

This section deals with the overall flow characteristics inside the rotor-stator cavity, and the similarities and deviations between the RANS and time-averaged WMLES results are discussed. To avoid unnecessary repetitive descriptions, only the c_w=2500 case is discussed in detail in this section; the influence of the increased radial throughflow rate in the cavity flow characteristics will be discussed later.

The rotating fluid motion is dominated by two important nondimensional parameters: (a) the Ekman number indicating the relative strengths of viscous force and Coriolis force, and (b) the Rossby number indicating the relative strengths of sealing flow inertia force and rotational inertia force. The Ekman number Ek and Rossby number Ro are defined using the following equations:

$$Ek=\frac{\upsilon}{\Omega b^2}, \tag{2}$$

$$Ro=\frac{v_r}{\Omega b}, \tag{3}$$

where υ is the fluid viscosity, and v_r is the radial velocity component. Since v_r and the viscous force are

negligible outside the boundary layer region, Ek and Ro are far less than 0. Under this circumstance, the flow in the rotor-stator cavity abides by the Taylor-Proudman (T-P) theorem which states that the flow parameters are invariant along the rotating axis. The T-P theorem demonstrates the existence of a rigid rotating core inside the rotor-stator cavity, i.e., the Batchelor flow model.

The swirl ratio β (i.e., nondimensional circumferential velocity) and nondimensional radial velocity v_r^* profiles are extracted from the simulation results along the axial direction from the stator (x^*=0) to the rotor (x^*=1) at four different radial positions: r^*=0.3, r^*=0.5, r^*=0.7, and r^*=0.9. The nondimensional parameters x^*, r^*, β, and v_r^* are defined using Eqs. (4)–(7), and the corresponding radial positions are illustrated in Fig. 9.

$$x^* = \frac{x}{c}, \tag{4}$$

$$r^* = \frac{r-a}{b-a}, \tag{5}$$

$$\beta = \frac{v_\theta}{\Omega r}, \tag{6}$$

$$v_r^* = \frac{v_r}{\Omega r}, \tag{7}$$

where v_θ represents the circumferential velocity component.

The velocity profiles are plotted in Figs. 10 and 11. Both RANS and WMLES results indicate that a classic Batchelor flow mode is formed in the cavity regardless of the superimposed sealing flow and shows separated boundary layers and a rotating core;

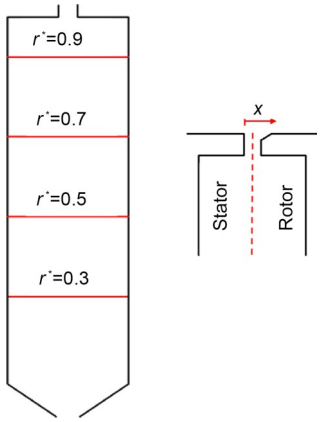

Fig. 9 Sampling position inside the rotor-stator cavity

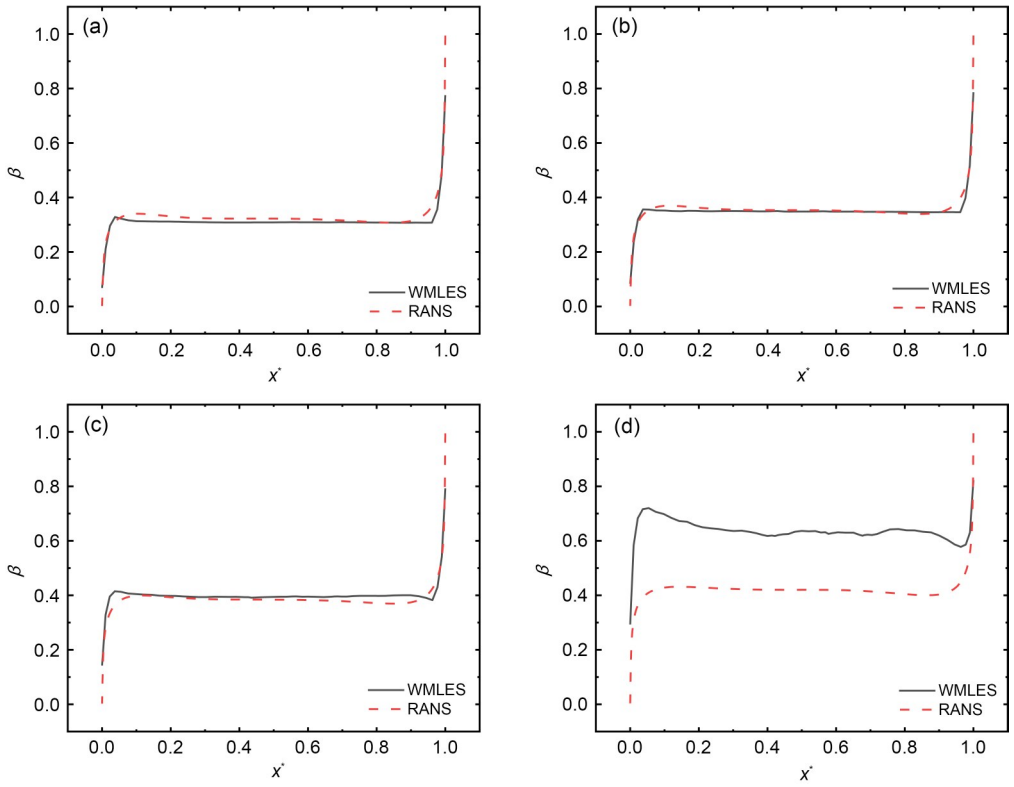

Fig. 10 Swirl ratio distributions in the rotor-stator cavity: (a) r^*=0.3; (b) r^*=0.5; (c) r^*=0.7; (d) r^*=0.9

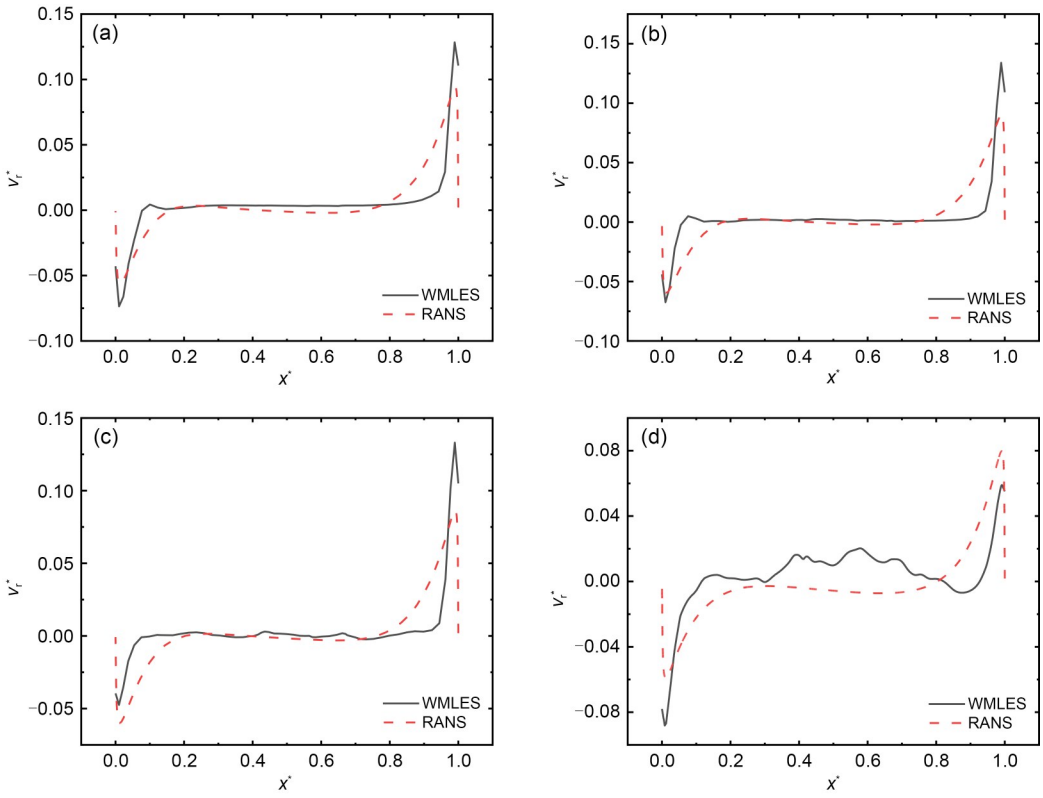

Fig. 11 Nondimensional radial velocity v_r^* distributions in the rotor-stator cavity: (a) r^*=0.3; (b) r^*=0.5; (c) r^*=0.7; (d) r^*=0.9

noticeable deviations are also observed between the RANS result and the WMLES result.

At lower radii, i.e., r^*=0.3, 0.5, and 0.7 in the current case, slight but noteworthy deviations are observed: (a) the swirl ratio in the WMLES approach is lower than that in the RANS approach, and (b) the WMLES boundary layer thickness is thinner than the RANS result. These deviations are not uncommon and were noticed in previous study (Palermo et al., 2020) and also in Fig. 5. The reason for this deviation at small radius is the grid resolution insufficiency of the RANS approach to capture the boundary layer vortical structures. The instantaneous Q-criterion contours are depicted both for RANS and WMLES approaches on a meridian plane in Fig. 12. The Q-criterion contour illustrates that the RANS simulation has over-filtered much of the disturbance in the boundary layers.

In the WMLES result, concentration of vorticity is observed both in rotor and stator boundary layers. These boundary layer vortical structures promote momentum exchanges between the boundary layer fluid and the rotating core. As a result, the swirl ratio in the WMLES result deviates from the steady RANS simulation result. Due to the intensified blending and mixing induced by these boundary layer vortices, the boundary layer thickness becomes thinner as seen in Fig. 11.

Another distinct deviation is observed in the large-radius region. As shown in Fig. 10d, the swirl ratio in the WMLES result is drastically higher than in the RANS result. Meanwhile, another vortical concentration region is observed at a large-radius region as shown in Fig. 12. These deviations can be attributed to the external crossflow ingress which arises from the different resolution of transportation equation in the RANS and WMLES simulations. The sealing effectiveness contour is shown in Fig. 13. As can be seen in the figure, nearly no ingress is observed in the RANS result, while a distinct ingress region is seen in the WMLES contour. Since the external crossflow is pre-swirled, when the crossflow is injected into the cavity, the cavity fluid is accelerated by the ingress air. As a result, the swirl ratio in the large-radius region is drastically higher than in the RANS result.

The boundary layer vortical structures and the mass convection process between the crossflow duct and the cavity causing these discrepancies will be discussed in Sections 3.2 and 3.3.

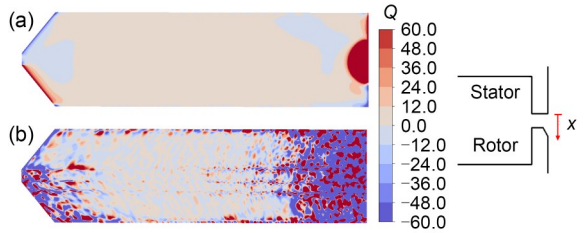

Fig. 12 Instantaneous Q-criterion contour on a meridian plane (Q is normalized by $\pi^2\Omega^2$): (a) RANS; (b) WMLES

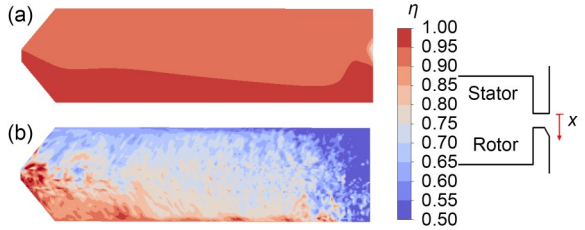

Fig. 13 Instantaneous sealing effectiveness η contour on a meridian plane: (a) RANS; (b) WMLES

As stated previously, the viscous effect and radial velocity can be neglected outside the boundary layer region. As a result, the main flow rotates as a rigid core and abides by the T-P theorem. However, at the near-wall region, where the viscous effect cannot be neglected, the flow is characterized by a spiral flow structure, i.e., the Ekman layer.

The thickness of the Ekman layer (δ_E) can be calculated using Eq. (8) (Childs, 2011), and the Ekman layer has an analytical solution of Eqs. (9) and (10) for laminar flows.

$$\delta_E = \sqrt{\frac{\upsilon}{\Omega}}, \tag{8}$$

$$v_\theta = U\left[1-\exp\left(-\frac{z}{\delta_E}\right)\cos\left(\frac{z}{\delta_E}\right)\right], \tag{9}$$

$$v_r = U\exp\left(-\frac{z}{\delta_E}\right)\sin\left(\frac{z}{\delta_E}\right), \tag{10}$$

where U is the mean flow velocity.

In the current case, the thickness of the Ekman layer calculated by Eq. (9) is 0.587 mm. The analytical solution of the Ekman layer and the velocity extracted from the simulation at different sealing flow rates are shown in Fig. 14. The radial velocity and relative circumferential velocity are nondimensionalized by the plate rotating speed Ωr. The solid line represents the analytical solution of the Ekman layer, and the dash-dot line indicates the isoline of $\frac{z}{\delta_E}$. All the velocity curves are drawn starting from $\frac{z}{\delta_E}=0$ to $\frac{z}{\delta_E}=3$. As can be seen in the figure, the velocity distributions all show a similar spiral distribution pattern under different sealing flow rates. Meanwhile, two distinct deviations are also observed.

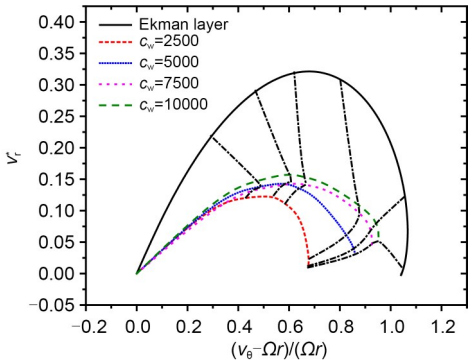

Fig. 14 Spiral velocity distribution pattern formed at different sealing flow rates at r^*=0.4 compared with the theoretical Ekman layer velocity distribution

Firstly, the radial and circumferential velocities are smaller than the analytical Ekman solution. This deviation stems from the difference in the far-field boundary condition. In the analytical analysis of the Ekman layer, the flow in the far-field is considered at rest, i.e., $v_r=0$, $|v_\theta-\Omega r|=\Omega r$. In the rotor-stator cavity case, due to the influence of the stator, the rotating core should be taken into consideration, so the far-field boundary condition is transformed to $v_r=0$, $|v_\theta-\Omega r|=(1-\beta)\Omega r$. As a result, due to the stalling effect of the stator, the velocity is smaller than the analytical solution.

Secondly, the velocity deviates from the analytical Ekman solution at $\frac{z}{\delta_E}=3$ where the analytical radial velocity is supposed to tend to 0. According to Eq. (10), the radial velocity is supposed to tend to 0 when $\frac{z}{\delta_E}$ tends to π while, under the influence of the imposed sealing flow, the velocity profiles extracted from simulation results have an increasing tendency at $\frac{z}{\delta_E}=3$ as the sealing flow rate increases.

As for the radial velocity distribution shown in Fig. 11, the same deviation is observed in terms of the

rotor boundary layer thickness, and the radial velocity distributions in RANS and WMLES coincide in most regions of the rotor-stator cavity while a large deviation is observed at the large-radius region. The radial ingress velocity at the stator plate is larger in the WMLES result compared to the RANS result, demonstrating an intensified ingress of external flow in WMLES. This discrepancy can also be attributed to the inertial momentum of the ingress air, as the analytical Ekman solution loses its applicability when the inertial momentum is not negligible.

As discussed above, the cavity flow is drastically influenced by the superimposed sealing flow and the external crossflow ingestion. Fig. 15 shows the axial distribution of swirl ratio and nondimensional radial velocity in the small-radius region (r^*=0.82) under different radial throughflow rates. The velocity distribution pattern conforms well with the classical Batchelor flow mode. When the sealing flow rate is increased, the core swirl ratio is decreased. The reason is that the superimposed sealing flow supplements the radial outflow induced by the rotor plate pumping effect. As a result, the cavity recirculation is suppressed and the swirl ratio of the rotating core is decreased. Meanwhile, when the sealing flow rate is increased, the rotor boundary layer region is expanded into the rotating core as shown in Fig. 15b.

In the large-radius region, as shown in Fig. 16 (r^*= 0.96), the flow pattern is strongly influenced by the external crossflow ingestion. The radial velocity basically conforms with the Batchelor flow mode, while a distinct deviation is observed in swirl ratio distribution as shown in Fig. 16a. The stator boundary layer swirl ratio is distinctly higher than the rotating core swirl ratio. The reason for this deviation is the external crossflow ingestion. When the crossflow is ingested into the cavity, it is directed into the stator boundary layer due to the boundary layer suction. Since the crossflow is pre-swirled, the fluid in stator boundary layer is accelerated by the ingested crossflow. As a result, the stator boundary layer swirl ratio is higher than that of the rotating core.

In summary, the RANS and WMLES results both resolved the Batchelor flow mode in the cavity. Due to the insufficiency of the RANS approach in capturing near-wall vortical structures and resolving

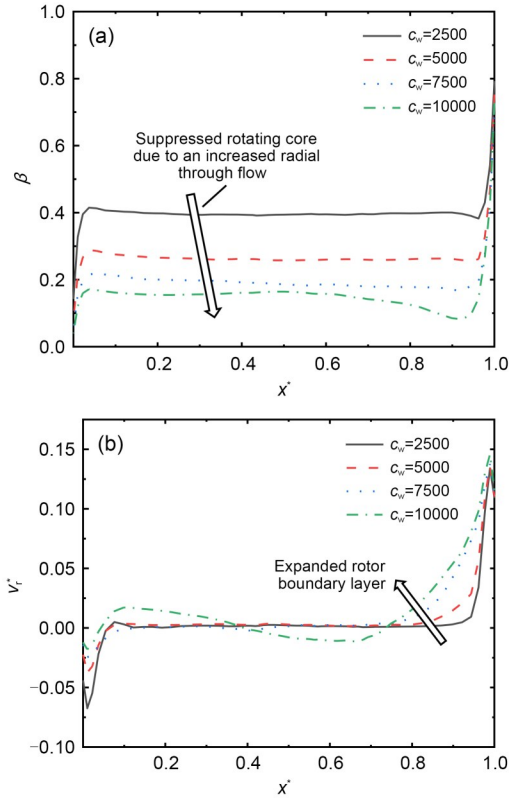

Fig. 15 Swirl ratio (a) and nondimensional radial velocity (b) axial distribution at r^*=0.82

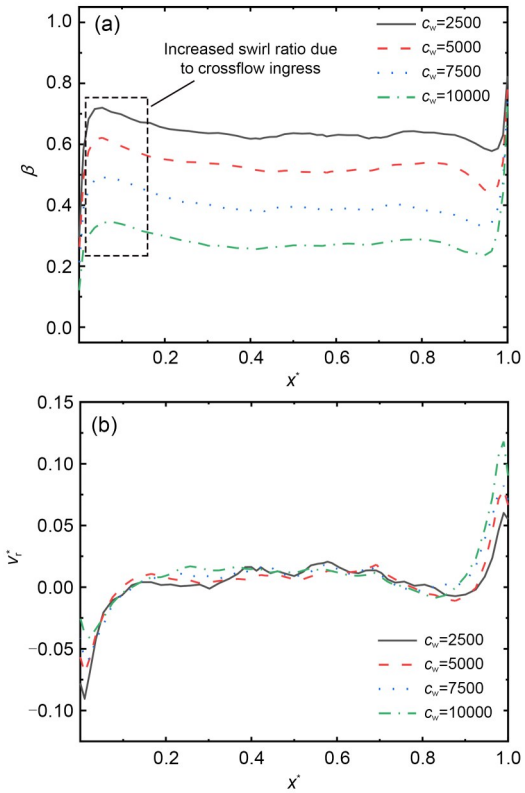

Fig. 16 Swirl ratio (a) and nondimensional radial velocity (b) axial distribution at r^*=0.96

the transportation equation, noticeable deviation exists. In the following sections we discuss the characteristics of these vortical structures and the mass transportation process based on WMLES results.

3.2 Boundary layer vortex and related flow instabilities

The disturbance and flow instability inside the rotor-stator cavity are the combined effects of external ingested air and the sealing flow. It can be divided into two main sources: (a) the blending of the ingress external air with the flow inside the cavity, and (b) the intrinsic instability induced by the rotating effect. These two sources of disturbance are related to three different kinds of flow instabilities: the centrifugal instability induced by rotation, the crossflow instability induced by 3D, and the K-H instability induced by velocity shearing.

This section deals with the intrinsic boundary layer vortex structure and its related flow instability. Since the large-radius region is strongly influenced by the external ingestion, only the first two kinds of rotating intrinsic instabilities in the low radius positions (i.e., r^*=0.3, 0.5, and 0.7) are discussed here. The K-H instability induced by external ingress is discussed in Section 3.3.

As discussed in the previous part, the vortical structure inside the cavity accounts for the deviation between steady RANS and unsteady WMLES simulation in the cavity small-radius region. The formation of vortical structures in the rotor-stator cavity is related to different kinds of flow instability.

Lingwood (1995) pointed out that there are three kinds of flow instabilities. Type I instability arises from the competition between the radial outflow induced by the rotor pumping effect and the circumferential flow induced by the rotation of the rotor plate; this is referred to as crossflow instability. The fundamental mechanism of this instability lies in the inflectional radial velocity distribution. As shown in Fig. 11, the radial velocity is inflectional due to the wall no-slip condition and the rotating core force balance. This kind of inflectional velocity distribution is absolutely unstable and amplifies the disturbances in the cavity. Type II instability is related to the disequilibrium of pressure gradient and the Coriolis force; it is referred to as centrifugal instability. Due to the accelerating and deaccelerating effect of the rotor and stator plates, the pressure gradient is lower or larger than the Coriolis force in both boundary layers. As a result, the fluid particle is naturally in an unstable state in both boundary layers, and the disturbances are amplified radially outward (rotor plate) or inward (stator plate).

In addition to those two classical instabilities, Lingwood (1995) found that there is an absolute instability in the whole cavity when the rotational Reynolds number reaches a certain value, which is referred to as Type III instability. When this kind of absolute instability is triggered, all kinds of disturbances will be amplified regardless of its position in the cavity.

Both Type I and Type II instabilities are related to the boundary layer vortex formation in the cavity. Type II centrifugal instability is related to the Görtler vortex formation as shown in Fig. 17a. Since the flow in the cavity is dominated by circumferential velocity, when the pressure gradient is insufficient or superfluous to offset the Coriolis force, a radial velocity component is induced. Consequently, the fluid particle flows in a spiral pattern and induces streamwise vortexes. Type I crossflow instability is related to the rolling up process in the boundary layer as shown in Fig. 17b. The mechanism of crossflow instability is similar to the classical K-H instability. The induced radial velocity component can be viewed as an extra shearing effect and induces a sheet of rolling up vortices in the boundary layer.

The overall instantaneous Q-criterion vorticity contour of the c_w=2500 case inside the cavity is depicted

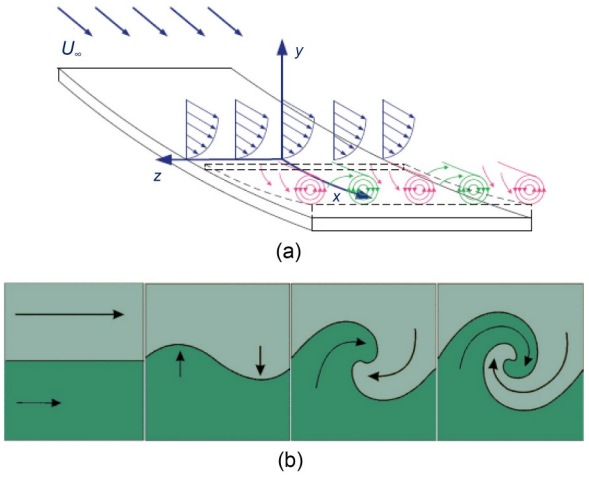

Fig. 17 Two different kinds of vortices induced by Type I and Type II instabilities: (a) centrifugal instability induced Görtler vortex; (b) crossflow instability induced rolling up vortex sheet. U_∞ is the inflow velocity

in Fig. 18. A sheet of streamwise-oriented and counter-rotating vortices is found in both rotor and stator boundary layers in the small-radius region which, according to Saric (1994), are the major distinguishing features of centrifugal instability induced Görtler vortices as shown in Fig. 17a.

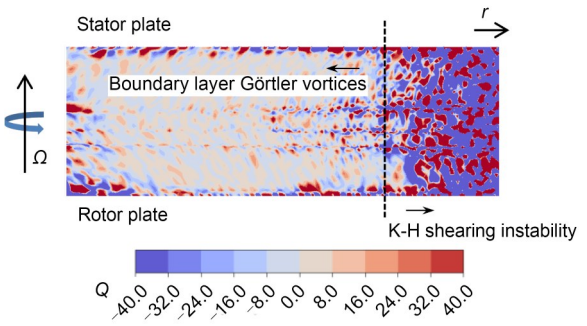

Fig. 18 Instantaneous *Q*-criterion vorticity contour inside the cavity (c_w=2500, *Q* is normalized by $\pi^2\Omega^2$)

The *Q*-criterion vorticity contours of other larger sealing flow rate cases are shown in Fig. 19. Due to the Ekman layer suction effect, the superimposed radial sealing flow is entrained in the rotor boundary layer. As the radial sealing flow rate increases, the velocity shearing in the rotor boundary layers becomes stronger. As a result, the vorticity in the rotor boundary layer becomes greater.

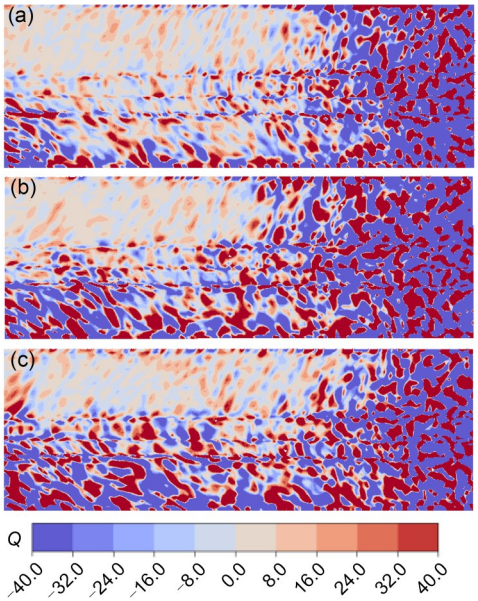

Fig. 19 Instantaneous *Q*-criterion vorticity contour inside the cavity under different sealing flow rates: (a) c_w=5000; (b) c_w=7500; (c) c_w=10000

The vortex structures introduce perturbations into the flow field, and these perturbations can be reflected in the turbulent kinetic energy (TKE). The TKE is defined to be half the trace of the Reynolds stress tensor $<v_i'v_j'>$, where the angle brackets represent the ensemble average process. It is the mean kinetic energy per unit mass in the fluctuating velocity field. The Reynolds equation indicating the momentum conservation can be written as Eq. (11), with ρ being the fluid density. As shown in the equation, the momentum transfer has three sources: (a) the isotropic stress $-<p>\delta_{ij}$ which stems from the mean pressure field, (b) the viscous stress $\upsilon\dfrac{\partial<v_i>}{\partial x_j}$ which stems from the molecular effect, and (c) the Reynold stress which stems from the fluctuating field. As a result, the blending process can be reflected by the TKE value since strong momentum transfer is induced by the mixing process.

$$\frac{\partial<\frac{1}{2}v_i>}{\partial t}+<v_j>\frac{\partial<v_i>}{\partial x_j}=-\frac{<p>}{\rho}\delta_{ij}+\frac{\partial}{\partial x_j}\left(\upsilon\frac{\partial<v_i>}{\partial x_j}-<v_i'v_j'>\right). \tag{11}$$

The boundary layer intrinsic instability induced streamwise vortices intensify the blending process between the rotating core and boundary layer fluids. The nondimensional axial, circumferential, and radial TKE components are plotted from the stator (x^*=0) to the rotor (x^*=1) at different radial positions as shown in Fig. 20.

The governing equation for TKE is shown in Eq. (12).

$$\frac{\partial<\frac{1}{2}v_i'v_i'>}{\partial t}+<v_k>\frac{\partial<\frac{1}{2}v_i'v_i'>}{\partial x_k}=-<v_i'v_k'>\frac{\partial<v_i>}{\partial x_k}-\frac{\partial}{\partial x_k}\left(<\frac{1}{2}v_i'v_i'v_k'>+\frac{<p'v_k'>}{\rho}-\upsilon\frac{\partial<\frac{1}{2}v_i'v_i'>}{\partial x_k}\right)+2\Omega\varepsilon_{ik3}<v_i'v_k'>-\upsilon<\frac{\partial v_i'}{\partial x_k}\frac{\partial v_i'}{\partial x_k}>. \tag{12}$$

The production term of TKE $<v_i'v_k'>\dfrac{\partial<v_i>}{\partial x_k}$ indicates a co-effect of mean velocity gradient and

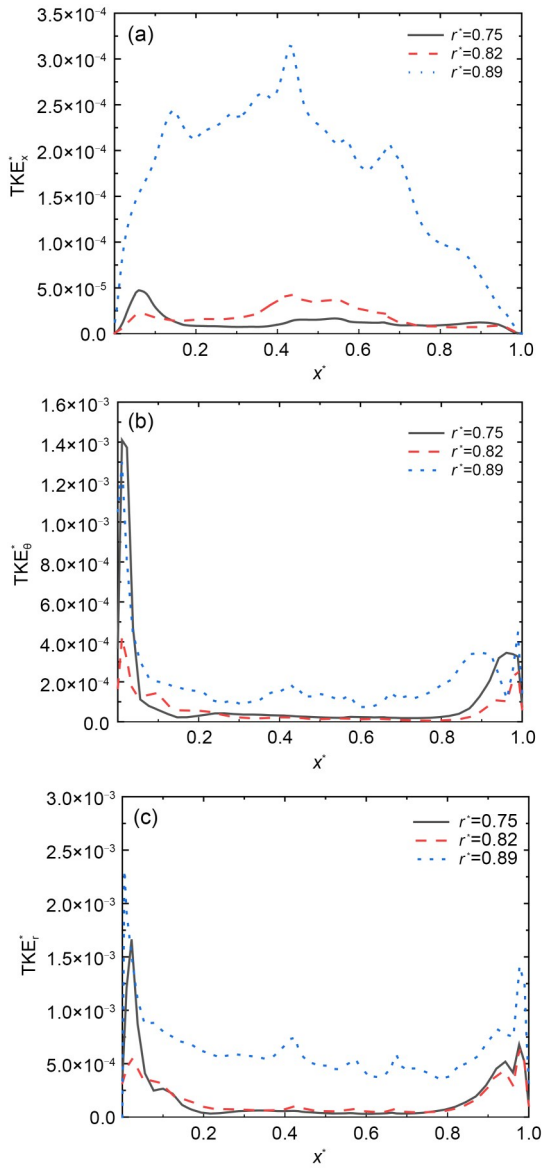

Fig. 20 Axial distribution of TKE distribution in cavity (c_w= 2500, and TKE is normalized by $\Omega^2 r^2$): (a) axial; (b) circumferential; (c) radial

turbulent Reynolds shear stress. As shown in Fig. 20, since the mean flow field is of the Batchelor type and the velocity gradient is 0 in the rotating core, the TKE value is relatively small in the rotating core while there is a relatively large TKE value in the boundary layer region, reflecting the influence of the boundary layer large velocity gradient and the boundary layer vortices which produce much of the turbulent shear stresses.

Since the mean axial velocity component gradient is relatively small compared to the other two components, the axial TKE value is an order lower than the other two components.

Another noticeable finding is that the TKE value in the stator boundary layer is relatively larger than in the rotor boundary layer, reflecting that the stator boundary layer is more unstable than the rotor boundary layer. This phenomenon was also reported by Lingwood (1995) in enclosed rotor-stator cavities. As a result, the blending process is stronger near the stator plate. This phenomenon explains why the WMLES predicted swirl ratio is lower than the RANS predicted results; the fluid rotating speed in the stator boundary layer is lower than in the rotating core.

The TKE at r^*=0.7 under different sealing flow rates is shown in Fig. 21. As the sealing flow rate increases, the TKE in the rotor boundary layer increases and becomes larger than in the stator boundary layer, while the TKE in the stator boundary layer decreases.

The increased sealing flow rate intensifies the crossflow instability and weakens the formation of the rotating core. As a result, the TKE is increased in the rotor boundary layer, reflecting the influence of intensified crossflow instability. However, due to the suppressed rotating core, the turbulent perturbation is decreased in the stator boundary layer.

3.2 Mass convection and related K-H instability

As previously presented, the cavity large-radius region is strongly influenced by the external crossflow ingress and the induced K-H instability. Fig. 22 shows the radial pressure difference and swirl ratio distribution in the computation domain in the c_w= 2500 case. The pressure at r^*=0.68 is selected as the reference pressure. As shown in Fig. 22a, a radial pressure gradient is formed inside the cavity due to centrifugal force while in the crossflow duct, since the crossflow flow rate is much larger compared to the cavity flow, the pressure in the duct is distinctly higher than the cavity pressure. As a result, a pressure difference is observed in the sealing gap as shown in Fig. 22a. Under the effect of that pressure difference, the crossflow is ingested into the cavity, causing an inverse pressure gradient in the rim sealing gap, as indicated in the box in r^*=0.98–1.02.

Once the ingestion has occurred, a velocity shearing layer is formed in the rim sealing gap as shown in Fig. 22b. The velocity shearing layer forms a surface vortex in the sealing gap as indicated in Fig. 23. The

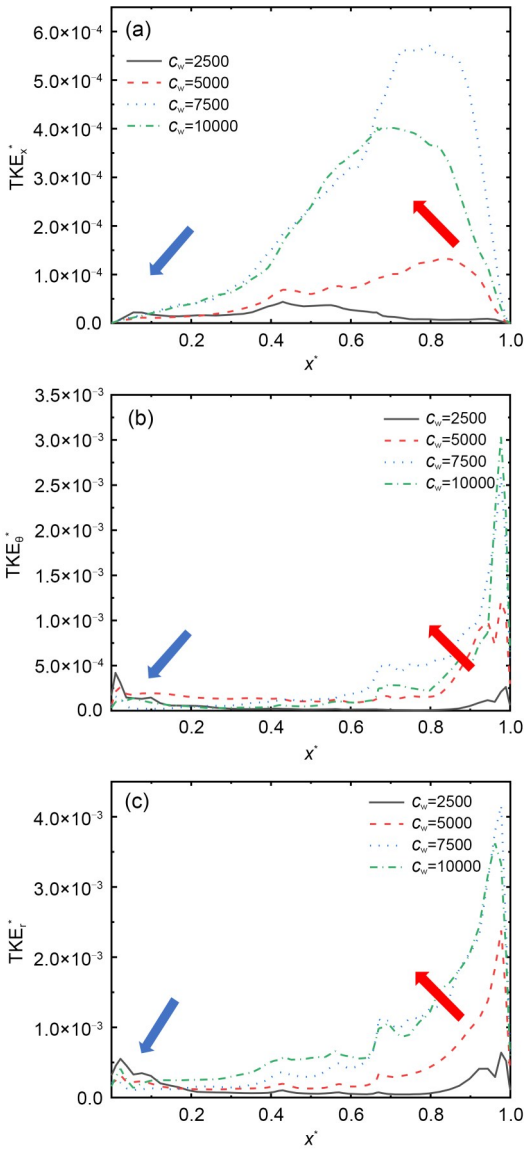

Fig. 21 Axial distribution of TKE distribution at r^*=0.7 (c_w=2500, and TKE is normalized by $\Omega^2 r^2$): (a) axial; (b) circumferential; (c) radial

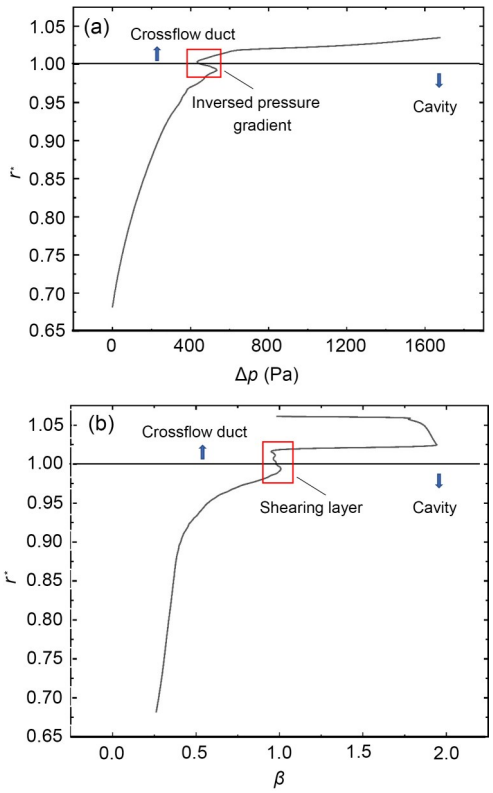

Fig. 22 Radial pressure difference Δp (a) and swirl ratio (b) in the computation domain (c_w=2500 case)

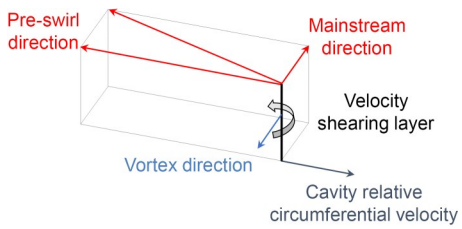

Fig. 23 Schematic sketch of the shearing layer in the sealing gap

surface vortex direction is opposite to the crossflow direction. According to stability theory, the surface vortex is absolutely unstable. Infinitesimal perturbations will destabilize the surface vortex and induce smaller vortex structures. This instability is the so-called K-H instability.

The iso-surface of a *Q*-criterion vortex structure inside the computation domain is shown in Fig. 24 both in a front view and a vertical view. To identify the rolling direction of these vortex structures, they are also colored by the nondimensional radial velocity. As shown in Fig. 24, discontinuous vortex structures are formed inside the sealing gap, and the rolling direction is the same as the surface vortex, as shown in Fig. 23, demonstrating that these vortexes are induced by the unstable surface vortex sheet. These discontinuous vortex structures induce radial inflow and outflow in the sealing gap as shown in Fig. 25.

The radial sealing flow also plays an important role in external ingestion and the related K-H instability. Vortex structures are rolled up in the velocity shearing layer, causing radial migration and strong blending between the crossflow and the cavity flow. This shearing and blending process is mainly observed in the large-radius region, so only the r^*>0.9 region is discussed in this part. To visualize the K-H instability

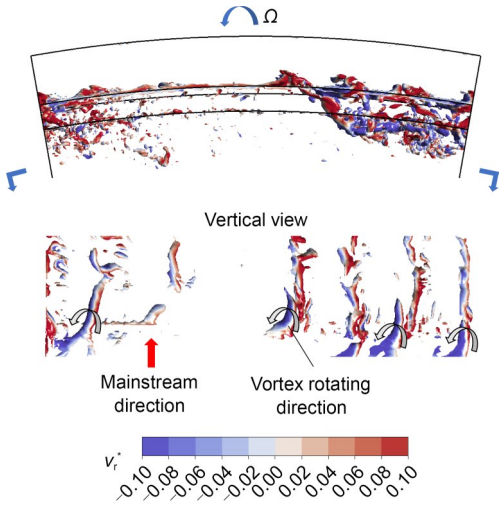

Fig. 24 Front and vertical views of the K-H vortex structures in the rim sealing gap. References to color refer to the online version of this figure

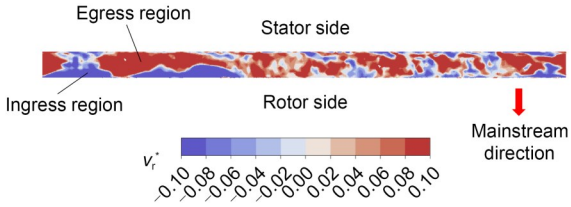

Fig. 25 Nondimensional radial velocity in the sealing gap. References to color refer to the online version of this figure

induced vortex structures in the cavity large-radius region, iso-surfaces of the Q-criterion under different sealing flow rates are shown in Fig. 26. The iso-surfaces are colored by swirl ratio to visualize the shearing effect since the swirl ratio is drastically different in the external annulus and cavity. As shown in Fig. 26, distinct large-scale vortex structures are resolved in the rim sealing region and radial migration is reflected by the swirl ratio of these vortex structures. As shown in Fig. 26a, the swirl ratio of the vortex structures in the cavity large-radius region is higher than 1.0, reflecting that these vortex structures are composed of ingested external crossflow fluids. However, in Fig. 26d, the swirl ratio of the vortex structure in the cavity is obviously lower than 0.5, indicating that the vortex is formed by the fluid in the cavity and little external crossflow is ingested. As the sealing flow rate increases, the vortex scale becomes smaller due to increased shearing instability.

The radial swirl ratios under different sealing flow rates are shown in Fig. 27. As the sealing flow

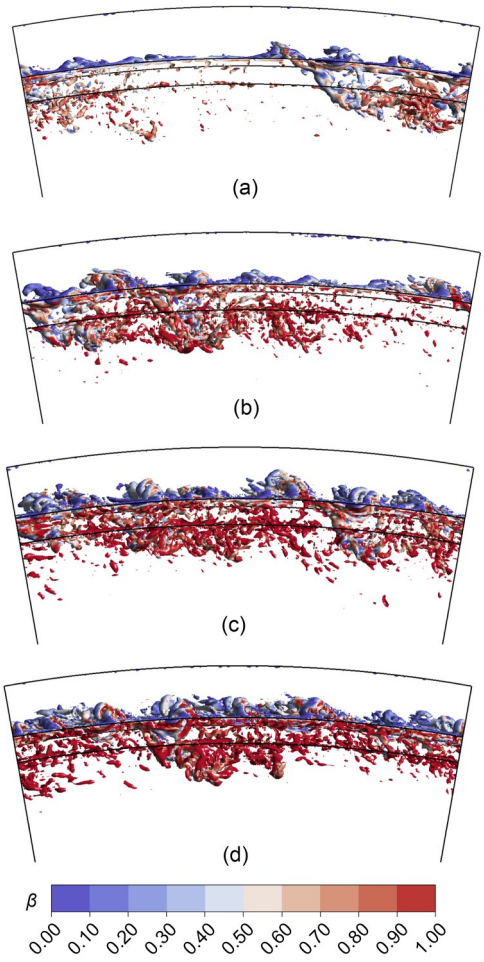

Fig. 26 Instantaneous Q-criterion iso-surface showing the K-H vortex ($Q/(\pi^2\Omega^2)$=15000 colored by swirl ratio): (a) c_w=2500; (b) c_w=5000; (c) c_w=7500; (d) c_w=10000. References to color refer to the online version of this figure

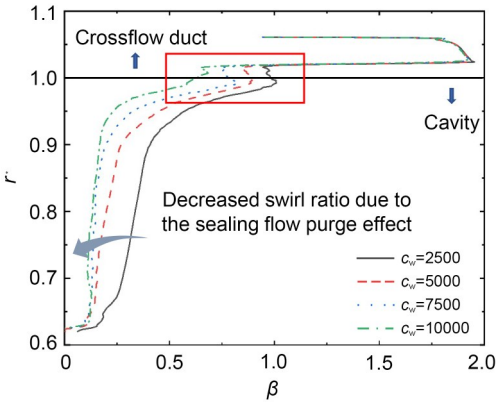

Fig. 27 Radial swirl ratio distribution inside rotor-stator cavity at x^*=0.5

rate increases, the cavity swirl ratio shown in Fig. 27 decreases, and thus the intensity of the shearing layer

becomes stronger. As a result, the amount of the vortex structure increases as the sealing flow rate increases as indicated in Fig. 26. The radial position of these vortex structures is also lifted by the superimposed sealing flow. When the sealing flow is relatively small, the flow in the sealing gap is dominated by external ingress, and the shearing layer is formed inside the cavity. When the sealing flow rate increases, the outflow in the sealing gap becomes stronger and the position of the shearing layer is also lifted. As can be seen in Fig. 26a, the vortex structures are mainly distributed in the sealing gap, while in Fig. 26d, the vortex structures are lifted and mainly distributed in the crossflow duct.

As stated previously, the blending process between the annulus and the cavity flow can be reflected by the TKE distribution. As shown in Fig. 28, it differs from the TKE distribution in the small-radius region as shown in Figs. 20 and 21; rather than sustaining a decimal value in the rotating core, the TKE value has a large value in the core region. Also, the axial TKE value is drastically increased to the same order as the circumferential and radial TKE. This TKE distribution pattern indicates that the flow is highly unstable and 3D under the influence of shearing K-H instability.

The strength of K-H instability is controlled by two factors: (a) the amount of ingress external air, and (b) the velocity difference. These two factors are counter-coupled by the sealing flow rate in a counter-acting effect. When the sealing flow rate is increased, the velocity shearing becomes stronger due to a suppressed rotating core, while the external ingress is suppressed since the cavity is pressurized by the sealing flow. As a result, the strength of K-H instability has a presumed maximum value as the sealing flow rate increases. When the cavity is nearly fully purged, little ingress is observed and the K-H instability vanishes inside the rotor-stator cavity. As shown in Figs. 28a–28d, the TKE value increases with the sealing flow rate when c_w<7500, while it is drastically decreased in the c_w=10000 case.

The counter-couple effect of the sealing flow can be visualized by the circumferential TKE contours under different sealing flow rates at r^*=0.9 as shown in Fig. 29. As can be seen in the figure, the TKE value

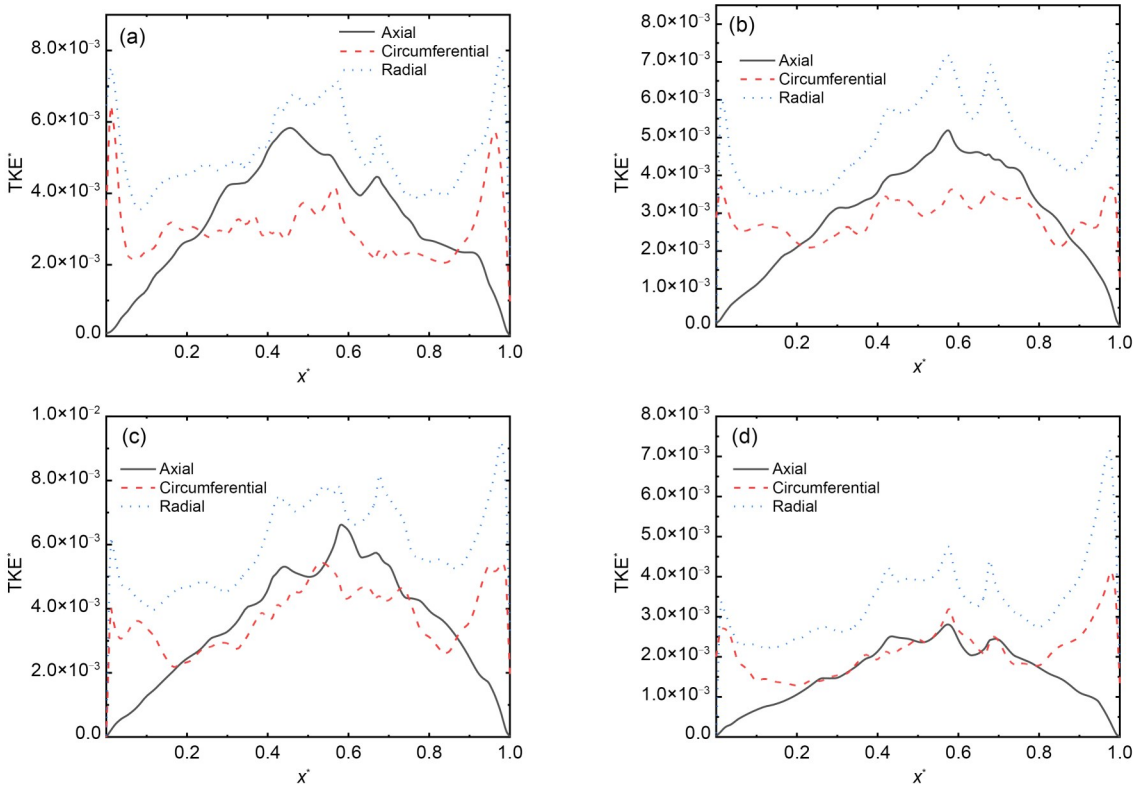

Fig. 28 TKE axial distribution at r^*=0.9 (TKE is normalized by $\Omega^2 r^2$): (a) c_w=2500; (b) c_w=5000; (c) c_w=7500; (d) c_w=10000

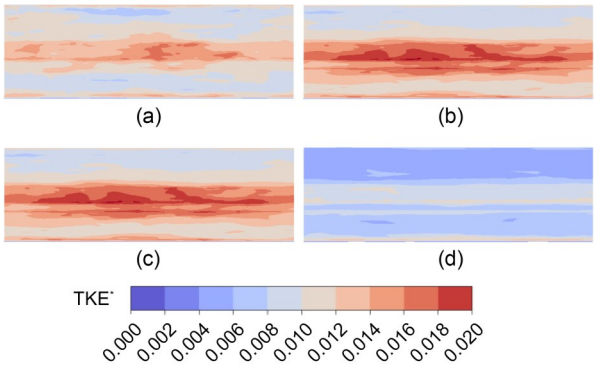

Fig. 29 TKE contour inside rotor-stator cavity at a r^*=0.9 iso-surface (TKE is normalized by $\Omega^2 r^2$): (a) c_w=2500; (b) c_w=5000; (c) c_w=7500; (d) c_w=10000

increases from the c_w=2500 case to the c_w=7500 case, while a sharp decrease is found in the c_w=10000 case in which little external ingress air is observed.

The radial velocity contour nondimensionalized by the rotor rotating speed at different sealing flow rates is shown in Fig. 30. As can be seen in the figure, a staggered distribution of the ingress region ($v_r^* < 0$) and the egress region ($v_r^* > 0$) is observed in all cases, which conforms with the characteristics of K-H vortices; the egress region prevails with the increase of sealing flow rate.

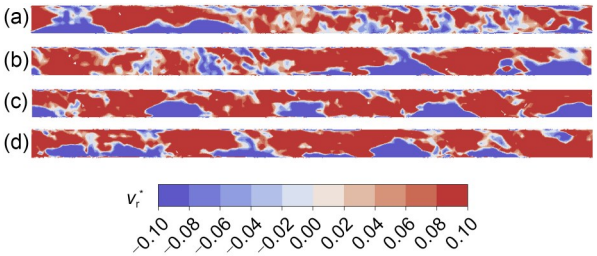

Fig. 30 Nondimensional radial velocity contour in the seal gap at r^*=1: (a) c_w=2500; (b) c_w=5000; (c) c_w=7500; (d) c_w=10000

The sealing effectiveness contour on a meridian plane is shown in Fig. 31. The typical Batchelor flow mode mentioned previously within the cavity involves two boundary layers separated by an inviscid rotating core. The sealing flow is entrained into the rotor boundary layer to compensate for the radial outflow induced by the rotation pumping effect. The ingress air flows into the cavity and is blended with the cavity flow under the effect of K-H instability in the cavity large-radius region and is directed inwards along the stator plate. As a result, the ingress region inside the

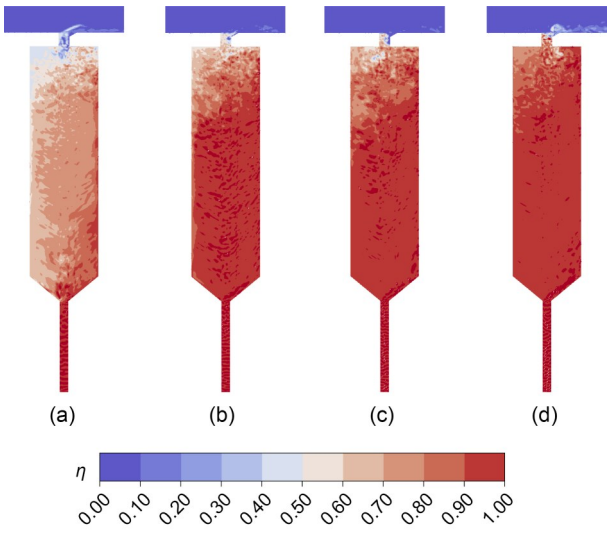

Fig. 31 Sealing effectiveness contour inside the rotor-stator cavity at a meridian plane: (a) c_w=2500; (b) c_w=5000; (c) c_w=7500; (d) c_w=10000

rotor-stator cavity shows a triangular pattern as indicated in Fig. 31. As the sealing flow rate increases, the triangular region shrinks. This triangular-shaped ingress region has a 'buffering' effect on the rotor, protecting the rotor from the influence of ingress air.

3.4 Large-scale flow structures

The large-scale structures in the rotor-stator cavity have been reported by many researchers in previous studies. In this part we deal with the mechanism of the flow structures and discuss the dynamic characteristics of these flow structures when submitted to different radial sealing flow rates.

As has been discussed in previous sections, the pressure in the external crossflow duct is higher than in the cavity. As a result, the ingress region is pressurized by the ingested external air, and the cavity pressure in the large-radius region shows a high/low staggering pattern as shown in Fig. 32.

The K-H instability induced radial ingress flow and egress flow in the large-radius region are subjected to different force conditions due to the Coriolis force. The different force conditions for ingress and egress air are shown in Fig. 33. In the figure, $\boldsymbol{v}_e$ represents the radial egress velocity, $\boldsymbol{v}_{in}$ represents the ingress velocity, and $\boldsymbol{v}_{\theta,rel}$ represents the relative circumferential velcocity. For egress air, the radial egress velocity $\boldsymbol{v}_e$ directs radially outwards, thus the resultant velocity $\boldsymbol{v}_{res,rel}$ also directs outwards as shown in the

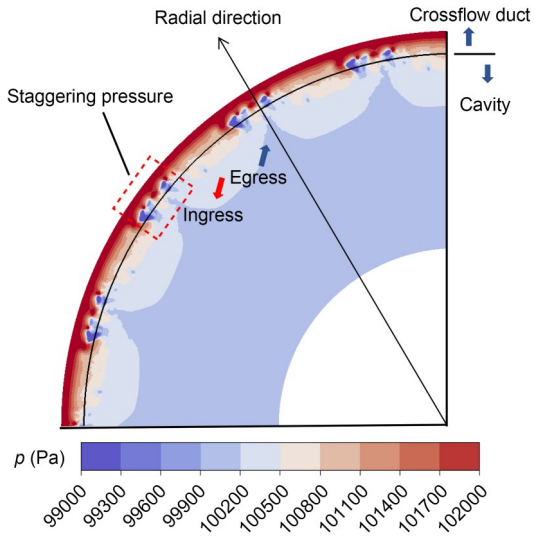

Fig. 32 High/low staggering pressure distribution pattern in the cavity

left velocity triangle in Fig. 33. The Coriolis force $\boldsymbol{f}_{c,r}$ is perpendicular to $\boldsymbol{v}_{res,rel}$, and it directs to the cavity inside while the driving pressure difference $\boldsymbol{f}_p$ of egress air is directed radially outwards. As a result, under the mutual performance of Coriolis force $\boldsymbol{f}_{c,r}$ and the pressure difference $\boldsymbol{f}_p$, the egress air shows a motion of fluctuation, which is a kind of inertia wave. As a result, the fluctuation of egress air strengthens the staggering pressure distribution pattern inside the cavity.

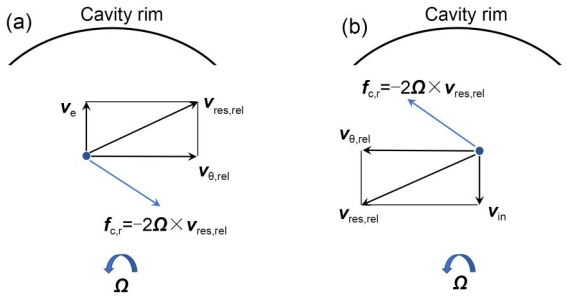

Fig. 33 Different force conditions for ingress and egress air: (a) radial egress; (b) radial ingress

Fig. 34 shows the sealing effectiveness contour at different sealing flow rates and reflects the blending and transmission process inside the rotor-stator cavity. The spiral flow structure can be distinctly identified in the contour. The spiral flow structure can be viewed as a pressure disturbance inside the rotor-stator cavity. The rotating speed and the number of the spiral flow structure can be calculated using the pressure oscillation wave.

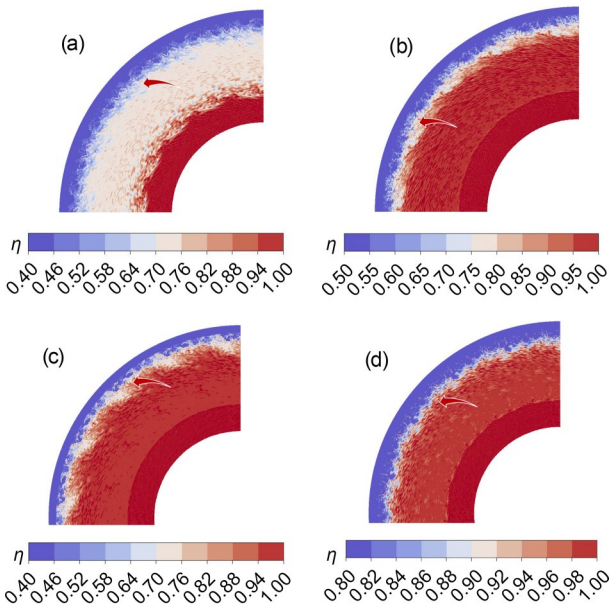

Fig. 34 Instantaneous sealing effectiveness contour inside the rotor-stator cavity at x^*=0.8 plane: (a) c_w=2500; (b) c_w=5000; (c) c_w=7500; (d) c_w=10000

The mechanism for computing the rotating speed and the number of the flow structure is shown in Fig. 35 (Gao et al., 2020). Two monitors separated by a known angle θ_1 are inserted inside the rotor-stator cavity (labeled probe 1 and probe 2 in Fig. 35). As the spiral structures flow past the two monitors, the pressure oscillation is recorded separately with a phase lag Δt_1 which can be calculated using cross-correlation coefficient R. Based on the obtained phase lag, the rotating speed of the flow structure ω_s can be obtained using Eq. (13). At the same time, the number of the flow structure N can be calculated using Eq. (14)

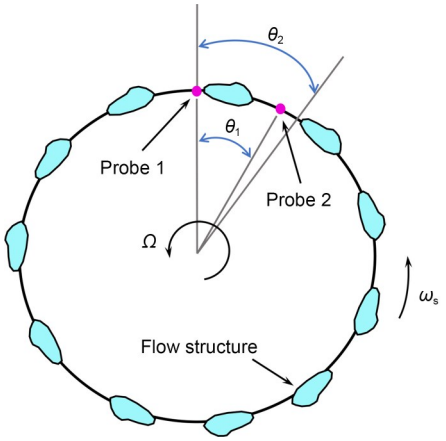

Fig. 35 Schematic diagram of flow structures inside wheel space cavity (Gao et al., 2020)

involving the main frequency f of the pressure oscillation wave. The main frequency f can be obtained by implementing fast Fourier transform (FFT). A detailed description of this cross-correlation method can be found in (Xie et al., 2021).

$$\omega_s = \frac{\theta_1}{\Delta t_1}, \tag{13}$$

$$N = \frac{360 f \Delta t_1}{\theta_1}. \tag{14}$$

The pressure oscillation waves at different sealing flow rates are shown in Fig. 36. As can be seen in the figure, a phase lag is observed in the c_w=2500, 5000, and 7500 cases, but it is absent in the c_w=10000 case. The absence of phase lag in the c_w=10000 case implies that there is no such spiral flow structure in the cavity.

The pressure oscillation waves are subjected to cross-correlation and FFT analysis. The phase lag Δt_1 between the pressure oscillation waves and the pressure wave main frequency f under different sealing flow rates is obtained and shown in Fig. 37. Using the obtained figures, the rotating speed and number of the flow structures are calculated at different sealing flow rates and are listed in Table 6. The pressure contour is also plotted inside the rotor-stator cavity demonstrating the existence of the spiral flow structure. The flow structure numbers listed in Table 6 coincide with the lobe structure in the pressure contour.

As listed in Table 6, the rotating speed of the flow structure decreases as the sealing flow rate increases, and it disappears when the sealing flow rate reaches c_w=10000. When the sealing flow rate is increased, the radial outflow induced by the rotor pumping effect is supplemented by the sealing flow rate, so the sealing flow rate stabilizes the flow inside the cavity and prevents the formation of the flow structure.

Meanwhile, by looking at the lobe structures in the pressure contour as shown in Fig. 38, the lobe structure is circumferential-dominated at a low sealing flow rate. As the sealing flow rate increases, the lobe structure develops radially due to the entrainment effect of the radial sealing flow.

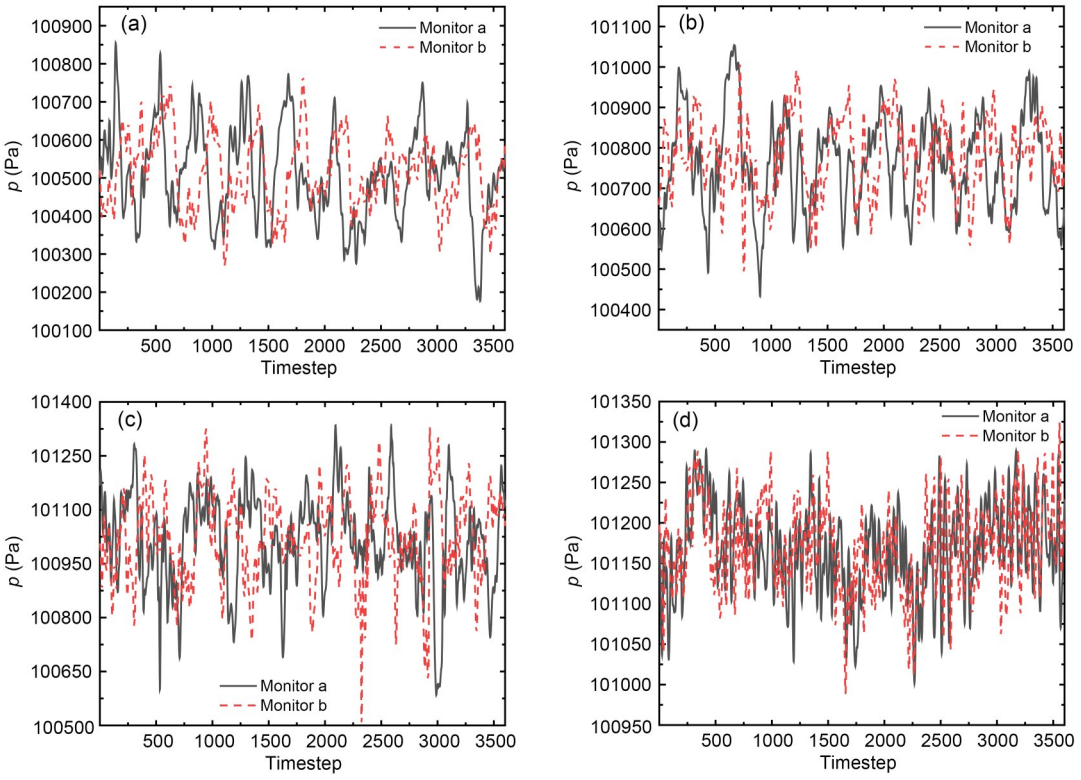

Fig. 36 Pressure oscillation wave inside rotor-stator cavity under different sealing flow rates: (a) c_w=2500; (b) c_w=5000; (c) c_w=7500; (d) c_w=10000

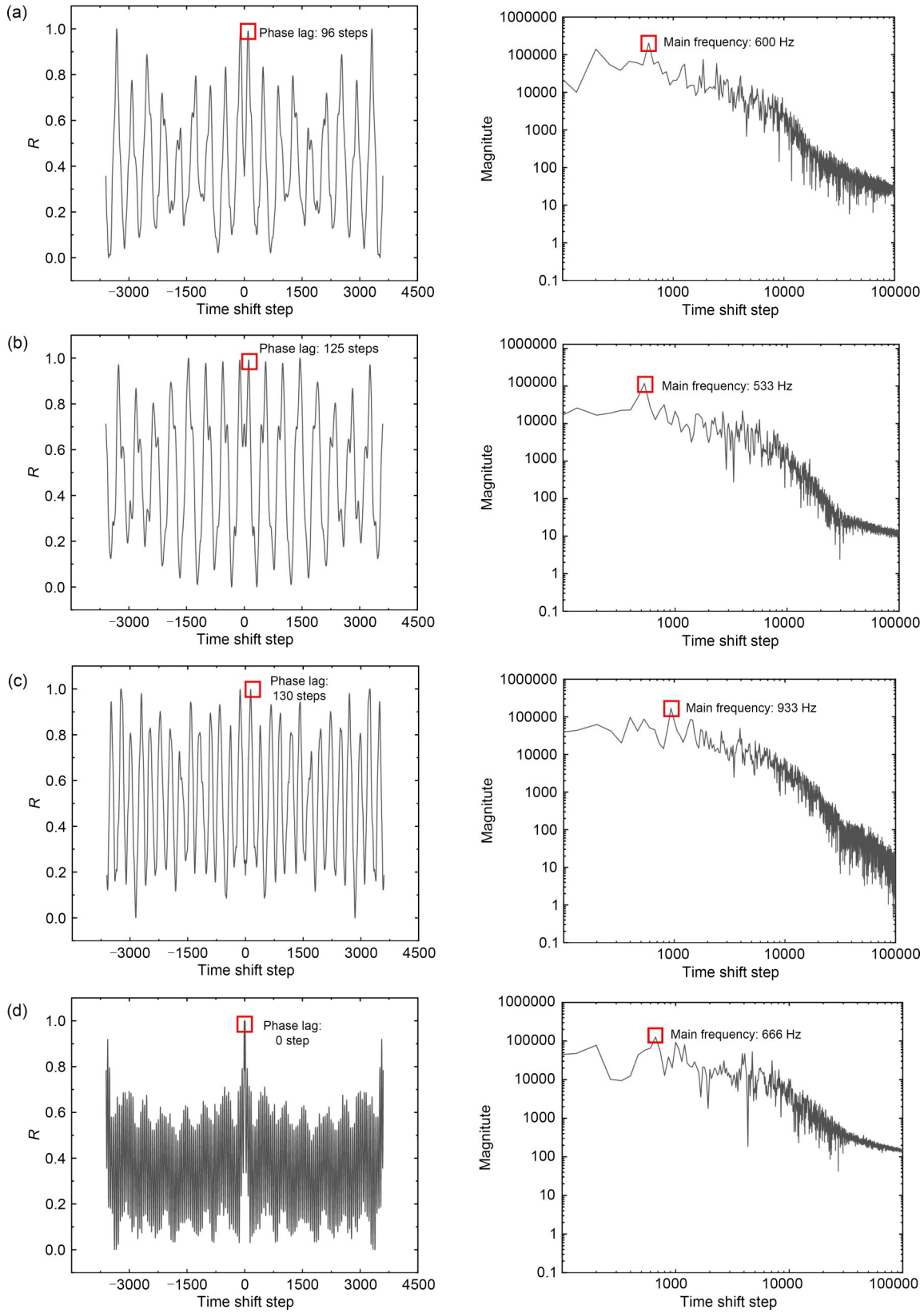

Fig. 37 Pressure fluctuation FFT results and cross-correlation coefficients: (a) c_w=2500; (b) c_w=5000; (c) c_w=7500; (d) c_w=10000

Table 6 Rotating speed and number of the flow structures

Sealing flow rate	Rotating speed (r/min)	Flow structure number
c_w=2500	2083	17.3
c_w=5000	1653	18.2
c_w=7500	1538	36.3
c_w=10000	0	0

4 Conclusions

The WMLES is used to investigate the flow characteristics in a rotor-stator cavity subjected to a pre-swirled external crossflow and radial sealing flow. The simulation is conducted using a 20° sector model in a relative frame of reference, and the unsteady WMLES simulation is triggered by a convergent RANS result.

The RANS and WMLES time-averaged results are compared. The velocity distributions in RANS and WMLES results show good agreement in most regions, but a notable deviation is observed in the large-radius region. Moreover, the cavity sealing efficiency distribution also shows large deviation. The reason for these deviations can be attributed to the insufficiency of the RANS approach in capturing boundary layer flow instabilities and in resolving the transportation equation properly. The perturbances in the near-wall and large-radius regions are over-filtered and the ingress is not properly predicted in the RANS approach. Since the superimposed sealing flow is directed into the rotor boundary layer, when the sealing flow rate is increased, the formation of the rotating core is suppressed, and the rotor boundary layer is expanded.

The near-wall streamwise vortices are discussed in detail based on WMLES results. These streamwise vortices are induced by crossflow instability and centrifugal instability, and strengthen the momentum convection between the rotating core and boundary layer fluids. Perturbations are induced by boundary layer vortex, causing a TKE peak in both boundary layers. When the sealing flow rate is increased, the TKE in the rotor boundary layer increases while in the stator boundary layer decreases due to the suppressed rotating core.

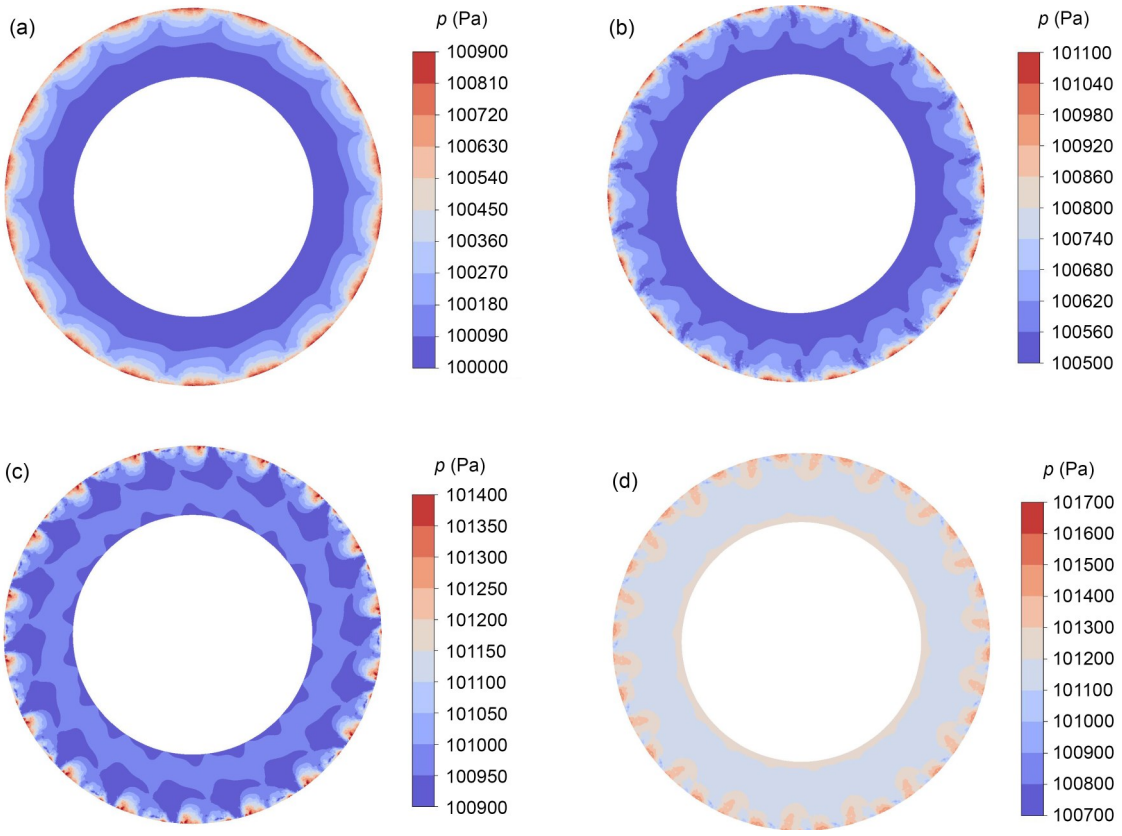

Fig. 38 Instantaneous pressure contour at x^*=0.8 plane: (a) c_w=2500; (b) c_w=5000; (c) c_w=7500; (d) c_w=10000

External crossflow ingress is observed in the cavity. The ingress is driven by the pressure difference between the cavity and the crossflow duct. A shearing layer is thus formed in the sealing gap, and K-H instability is induced at the cavity large-radius region. The K-H instability causes strong perturbations in the flow field, which is reflected by the large TKE value in the rotating core. Staggering distribution of ingress and egress regions is found in the rim seal gap and conforms to the characteristics of K-H vortices.

The K-H instability is a result of the external ingress and velocity shearing, and these two factors influence each other in opposite directions through the sealing flow rate. Increasing the sealing flow rate decreases the ingress of cavity air. Consequently, the strength of K-H instability is presumed to reach a maximum value as the sealing flow rate increases.

Meanwhile, due to the K-H shearing instability, ingress is still observed in the large sealing flow rate case. The ingress air is blended with the cavity flow in the large-radius region under the effect of K-H vortices and flows inwards along the stator plate, forming a triangular ingress area inside the cavity. This triangular ingress air protects the rotor plate from the harm of external ingested air.

Large-scale flow structures are observed in the rotor-stator cavity due to the different force conditions of the ingress and egress air. A cavity high-pressure region is induced by external ingress, and as a result the pressure distribution in the cavity large-radius region shows a high/low staggering pattern. The high/low pressure staggering distributed flow structure is found to be rotating at a certain speed, and the rotating speed and lobe number of the flow structure can be determined using cross-correlation and FFT.

Acknowledgments

This work is supported by the National Natural Science Foundation of China (No. 5212201273) and the National Science and Technology Major Project of China (No. J2019-III-0003). The CFX software and computation resource supplied by Beijing Super Cloud Computing Center, China are acknowledged.

Author contributions

Qiang DU designed the research. Guang LIU and Zengyan LIAN processed the corresponding data. Lei XIE wrote the first draft of the manuscript. Yaguang XIE helped to organize the manuscript. Lei XIE and Yifu LUO revised and edited the final version.

Conflict of interest

Lei XIE, Qiang DU, Guang LIU, Zengyan LIAN, Yaguang XIE, and Yifu LUO declare that they have no conflict of interest.

References

Bayley FJ, Owen J, 1970. The fluid dynamics of a shrouded disk system with a radial outflow of coolant. *Journal of Engineering for Gas Turbines and Power*, 92(3):335-341. https://doi.org/10.1115/1.3445358

Bhavnani SH, Khilnani VI, Tsai LC, et al., 1992. Effective sealing of a disk cavity using a double-toothed rim seal. Proceedings of the ASME International Gas Turbine and Aeroengine Congress and Exposition, No. V001T01A127. https://doi.org/10.1115/92-GT-379

Childs PRN, 2011. Chapter 7: rotating cavities. *In*: Childs PRN (Ed.), Rotating Flow. Butterworth-Heinemann, Oxford, UK, p.249-298. https://doi.org/10.1016/B978-0-12-382098-3.00007-X

Gao F, Chew JW, 2021. Evaluation and application of advanced CFD models for rotating disc flows. *Proceedings of the Institution of Mechanical Engineers, Part C: Journal of Mechanical Engineering Science*, 235(23):6847-6864. https://doi.org/10.1177/09544062211013850

Gao F, Chew JW, Marxen O, 2020. Inertial waves in turbine rim seal flows. *Physical Review Fluids*, 5(2):024802. https://doi.org/10.1103/PhysRevFluids.5.024802

Georgiadis NJ, Rizzetta DP, Fureby C, 2010. Large-eddy simulation: current capabilities, recommended practices, and future research. *AIAA Journal*, 48(8):1772-1784. https://doi.org/10.2514/1.J050232

Horwood JTM, Hualca FP, Scobie JA, et al., 2019. Experimental and computational investigation of flow instabilities in turbine rim seals. *Journal of Engineering for Gas Turbines and Power*, 141(1):011028. https://doi.org/10.1115/1.4041115

Hualca-Tigsilema FP, 2020. An Experimental Study of Ingress Through Gas-Turbine Rim Seals. PhD Thesis, University of Bath, Bath, UK.

Jakoby R, Zierer T, Lindblad K, et al., 2004. Numerical simulation of the unsteady flow field in an axial gas turbine rim seal configuration. ASME Turbo Expo 2004: Power for Land, Sea, and Air, p.431-440. https://doi.org/10.1115/GT2004-53829

Larsson J, Kawai S, Bodart J, et al., 2016. Large eddy simulation with modeled wall-stress: recent progress and future directions. *Mechanical Engineering Reviews*, 3(1):15-00418. https://doi.org/10.1299/mer.15-00418

Lingwood RJ, 1995. Absolute instability of the boundary layer on a rotating disk. *Journal of Fluid Mechanics*, 299: 17-33. https://doi.org/10.1017/S0022112095003405

Nakhchi ME, Naung SW, Rahmati M, 2022. Influence of blade vibrations on aerodynamic performance of axial compressor in gas turbine: direct numerical simulation.

Energy, 242:122988.
https://doi.org/10.1016/j.energy.2021.122988

Naung SW, Nakhchi ME, Rahmati M, 2021. Prediction of flutter effects on transient flow structure and aeroelasticity of low-pressure turbine cascade using direct numerical simulations. *Aerospace Science and Technology*, 119:107151.
https://doi.org/10.1016/j.ast.2021.107151

O'Mahoney TSD, Hills NJ, Chew JW, et al., 2011. Large-eddy simulation of rim seal ingestion. *Proceedings of the Institution of Mechanical Engineers, Part C: Journal of Mechanical Engineering Science*, 225(12):2881-2891.
https://doi.org/10.1177/0954406211409285

Owen JM, 2011a. Prediction of ingestion through turbine rim seals—part I: rotationally induced ingress. *Journal of Turbomachinery*, 133(3):031005.
https://doi.org/10.1115/1.4001177

Owen JM, 2011b. Prediction of ingestion through turbine rim seals—part II: externally induced and combined ingress. *Journal of Turbomachinery*, 133(3):031006.
https://doi.org/10.1115/1.4001178

Owen JM, Zhou KY, Pountney O, et al., 2012a. Prediction of ingress through turbine rim seals—part I: externally induced ingress. *Journal of Turbomachinery*, 134(3):031012.
https://doi.org/10.1115/1.4003070

Owen JM, Pountney O, Lock G, 2012b. Prediction of ingress through turbine rim seals—part II: combined ingress. *Journal of Turbomachinery*, 134(3):031013.
https://doi.org/10.1115/1.4003071

Palermo DM, Gao F, Amirante D, et al., 2020. Wall-modelled large eddy simulations of axial turbine rim sealing. ASME Turbo Expo 2020: Turbomachinery Technical Conference and Exposition, No. V07CT14A015.
https://doi.org/10.1115/GT2020-14973

Phadke UP, Owen JM, 1988a. Aerodynamic aspects of the sealing of gas-turbine rotor-stator systems: part 1: the behavior of simple shrouded rotating-disk systems in a quiescent environment. *International Journal of Heat and Fluid Flow*, 9(2):98-105.
https://doi.org/10.1016/0142-727X(88)90060-4

Phadke UP, Owen JM, 1988b. Aerodynamic aspects of the sealing of gas-turbine rotor-stator systems: part 2: the performance of simple seals in a quasi-axisymmetric external flow. *International Journal of Heat and Fluid Flow*, 9(2):106-112.
https://doi.org/10.1016/0142-727X(88)90061-6

Phadke UP, Owen JM, 1988c. Aerodynamic aspects of the sealing of gas-turbine rotor-stator systems: part 3: the effect of nonaxisymmetric external flow on seal performance. *International Journal of Heat and Fluid Flow*, 9(2):113-117.
https://doi.org/10.1016/0142-727X(88)90062-8

Pogorelov A, Schneiders L, Meinke M, et al., 2018. An adaptive Cartesian mesh based method to simulate turbulent flows of multiple rotating surfaces. *Flow, Turbulence and Combustion*, 100(1):19-38.
https://doi.org/10.1007/s10494-017-9827-9

Rabs M, Benra FK, Dohmen HJ, et al., 2009. Investigation of flow instabilities near the rim cavity of a 1.5 stage gas turbine. ASME Turbo Expo 2009: Power for Land, Sea, and Air, p.1263-1272.
https://doi.org/10.1115/GT2009-59965

Royce R, 2015. The Jet Engine. 5th Edition. John Wiley & Sons Inc., Chichester, UK.

Sangan CM, 2011. Measurement of Ingress Through Gas Turbine Rim Seals. PhD Thesis, University of Bath, Bath, UK.

Sangan CM, Pountney OJ, Zhou KY, et al., 2013. Experimental measurements of ingestion through turbine rim seals—part I: externally induced ingress. *Journal of Turbomachinery*, 135(2):021012.
https://doi.org/10.1115/1.4006609

Saric WS, 1994. Görtler vortices. *Annual Review of Fluid Mechanics*, 26:379-409.
https://doi.org/10.1146/annurev.fl.26.010194.002115

Savov SS, Atkins NR, 2017. A rim seal ingress model based on turbulent transport. ASME Turbo Expo 2017: Turbomachinery Technical Conference and Exposition.
https://doi.org/10.1115/GT2017-63531

Savov SS, Atkins NR, Uchida S, 2017. A comparison of single and double lip rim seal geometries. *Journal of Engineering for Gas Turbines and Power*, 139(11):112601.
https://doi.org/10.1115/1.4037027

Scobie JA, 2014. An Experimental Study of Gas Turbine Rim Seals. PhD Thesis, University of Bath, Bath, UK.

Séverac É, Poncet S, Serre É, et al., 2007. Large eddy simulation and measurements of turbulent enclosed rotor-stator flows. *Physics of Fluids*, 19(8):085113.
https://doi.org/10.1063/1.2759530

Xie L, Du Q, Liu G, et al., 2021. Flow characteristics in turbine wheel space cavity. *Energy Reports*, 7:2262-2275.
https://doi.org/10.1016/j.egyr.2021.04.014